7-28-2024

Improving Biomimetic Passive Dynamics of a Quadruped Robot Hind Leg Hip Joint with a 3D Printed Torsion Spring

Haonan Zheng
Portland State University

Improving Biomimetic Passive Dynamics of a Quadruped Robot Hind Leg Hip Joint with a 3D Printed Torsion Spring

by

Haonan Zheng

A thesis submitted in partial fulfillment of the
requirements for the degree of

Master of Science
in
Mechanical Engineering

Thesis Committee:
Alexander Hunt, Chair
David Turcic
Chien Wern

Portland State University
2024

Abstract

The Agile and Adaptive Robotics Lab is interested in researching the neuromuscular control network of legged animal locomotion. To validate the lab's understanding of biological neural control, synthetic neural networks are developed and applied to biologically inspired legged robots. For a synthetic neural network to operate in the same manner as a biological neural network and produce the same locomotor behavior, the robot that the synthetic neural network is controlling must also mimic its biological counterpart. Previous research produced a quadruped robot hind leg designed with biomimetic passive dynamics by installing spring and damper pairs at each joint, however, an identified area of improvement was to decrease the spring rate of the hip spring. This paper explores new hip joint designs and new hip springs to address the previous concerns. Two manufacturing methods were assessed for the new hip spring: manually winding ASTM A228 steel wire, and 3D printing with Onyx. 3D printing was identified as the preferable manufacturing method, and the quadruped hip was redesigned to integrate the new springs. Relationships between 3D printed spring geometry and spring parameters were experimentally determined for use in future modifications to the robot leg dynamics with varying levels of success. The 3D printed spring proved to be a successful replacement for the metal hip spring to obtain biomimetic passive dynamics in the robot leg. Future work includes implementing a damper to the hip and possibly printing continuous fibers within the springs to improve spring performance repeatability.

Acknowledgements

I would like to thank Dr. Hunt for his guidance and insight throughout this project, and for fostering a great lab environment to research in. Thank you to Dr. Turcic and Dr. Wern for their time serving on my committee, and all the AARL lab members for creating a welcoming and supportive lab environment. Lastly, a special thank you to my partner Ariana for her encouragement and support throughout my degree.

Table of Contents

List of Tables

List of Figures

Chapter 1. Introduction

1.1. Motivation

Neural network controllers are quickly gaining interest in academia and commercial software. Recent studies in academia include developing synthetic neural networks as a control mechanism for legged locomotion [1], [4] with the intent to understand the workings of the biological system through replication. One method to verify that a synthetic neural network operates in the same manner as a biological neural network is to apply it to the same physical system and compare the resultant system dynamics. A multitude of complications surround the application of synthetic neural networks to biological animals, therefore a biomimetic robot frame must be used instead. The Agile and Adaptive Robotics Lab (AARL) is continuously developing a quadruped robot the size of a medium dog to fit the criteria for testing synthetic neural networks.

Previous work by Emma Krnacik, a member of the AARL, has produced a quadruped robot hind leg with a spring and damper pair at each joint for biomimetic passive dynamics [5]. A SolidWorks model of this leg is shown in Figure 1. Spring and damper pairs were chosen so the leg would exhibit similar behaviors to an anesthetized rat leg when given the same initial angular positions. The rat leg data used to determine the desired passive dynamics of the quadruped robot were provided by Dr. Matt Tresch. Data was collected by stimulating individual muscle groups on the rat leg with electrodes to contract the muscle and set the leg into an initial position. High speed cameras were then used to track the angular position of the hip, knee, and ankle as the stimulus was

released. There was no muscle activation in the rat leg response post-stimulus that was used to determine the desired quadruped robot spring and damper pairs, hence the name passive dynamics.

Differences in size scale between the rat and quadruped robot were addressed by increasing the time scale of the rat data by a factor of 2, the ratio of walking stride period between medium sized dogs and rats [3], [6]. The robot leg components were 3D printed with the nylon-carbon fiber composite Onyx from Markforged [7]. The leg has 3 degrees of freedom, with d-shaped shafts joining the limbs. Limb lengths and joint range of motion were modelled to resemble a medium sized dog. On the quadruped robot link 1 refers to the femur, link 2 the fibula and tibia, and link 3 the tarsals and metatarsals. An AMT103 encoder is installed at each joint to measure angular displacements of the links.

Once the passive dynamics of the robot leg match the biological data, braided pneumatic actuators (BPAs) from Festo will be added to the leg. The BPAs contract when pressurized with air, mimicking the function of muscles on an animal that contract to control active limb dynamics. With biomimetic actuation and passive dynamics on the quadruped robot, applying a biologically accurate synthetic neural network to the robot would result in leg dynamics similar to the animal it was modelled after.

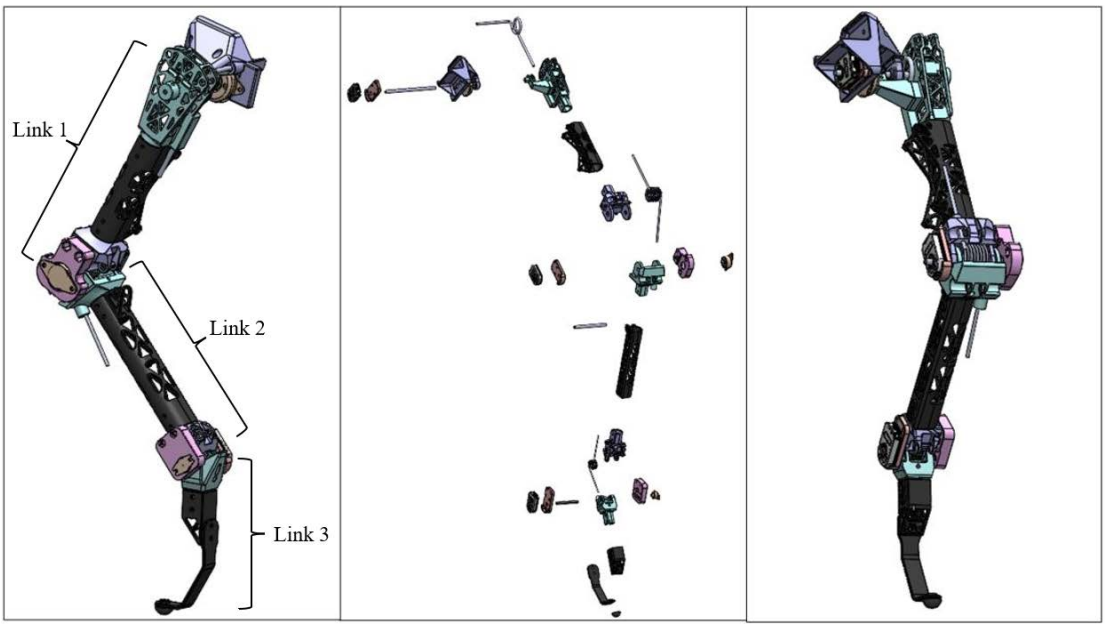

Figure 1: Quadruped robot hind leg with biomimetic passive dynamics

The leg with springs and dampers greatly improved biomimicry, however the spring rate of the hip spring was high, causing visible wear in the hip joint when twisted to its full range of motion. Due to the overdamped nature of the desired leg, a new spring and damper pair with less output torque could be selected to produce the same leg behavior and reduce wear on the physical frame of the leg.

To reduce the spring rate of the hip spring and maintain the robot leg's dynamics, a new damper with a lower damping constant also had to be selected. The experimental damping constant of the selected damper, and the subsequent desired spring rate to achieve biomimetic passive dynamics were determined following the same procedure outlined in Emma's thesis in sections 4.3.1 Damper Design and 4.3.2 Spring Design.

Stock rotary dampers have large differences in maximum torque between dampers making it the constraining component of the spring-damper pair, and had to be chosen first. The damper chosen was the continuous rotation, bidirectional rotary damper 6597K117 from McMaster Carr, with a maximum torque of 424.89 in-oz. This damper was chosen because it had the next smallest damping coefficient available on McMaster Carr. The new damper was installed on the quadruped robot hip with the knee and ankle joints locked at full extension so that the leg behaved as a single link. The quadruped leg was given an initial displacement and released, and the resultant angular position response was captured. The leg was modelled as a simple pendulum with a damper at the axis of rotation, and an optimizer script was used to calculate a damping constant that would result in the same pendulum dynamics as the robot leg data. The experimental damping constant of the 6597K117 was 0.81 Nms/rad, and a desired spring rate of 13.22 Nm/rad was calculated to pair with it for the desired leg dynamics using a separate optimizer script. To mimic a rat hind leg during locomotion, a 60° range of motion [2] in the quadruped robot hip is also desired.

1.2. Overview

Chapter 2 discusses the attempt to manufacture a metal hip spring to replace the existing metal hip spring. The new metal spring was manufactured to have a spring rate of 13.38 Nm/rad, and the existing damper was replaced with the new damper with an experimental damping constant of 0.81 Nms/rad. A new hip joint was designed and

manufactured to incorporate the new spring and damper. The passive dynamics of the new leg were tested by giving it the same initial conditions as the rat leg data and recording the angular position of each limb after the leg was released. There was no visible wear on the new robot hip joint after the trials and the new leg still exhibited biomimetic passive dynamics. One major difference between the robot leg and the rat leg was the settling position of the hip, which stemmed from dimensional inaccuracies in manufacturing the hip spring. New hip springs 3D printed with Onyx were considered to address this.

Chapter 3 discusses an attempt to manufacture the hip spring out of Onyx. with Chapters 3.2, 3.3, and 3.4 each detailing different testing methods to determine the Onyx spring parameters. Onyx is a nylon base material and chopped carbon fiber that is readily available in the AARL and was chosen for its high flexibility and toughness. 3D printing as a manufacturing method was considered for high dimensional accuracy and ease of manufacturing over steel springs. An adjustable 3D printed spring was initially desired to correct any modelling errors in desired spring rate without disassembling the robot leg, and to enable quick changes in stiffness to test hypotheses on the effect of stiffness on neural control. Early prototyping suggested this concept would require small, complex machined parts to work, potentially complicating future maintenance, and making the design less desirable. A hip with an accessible and modular hip spring design was pursued instead.

Chapter 3.2 discusses early testing which confirmed that 3D printed springs could meet the spring rate and range of motion requirements for the quadruped hip joint and

warranted further exploration. The project then focused on identifying a relationship between 3D printed spring geometry and spring rate. This relationship would allow members of the lab to configure multiple springs in parallel on the hip to change the overall spring rate. Performance of the quadruped leg could then be adjusted with minimal delays. The 3D printed springs showed significant damping properties, which prompted a damping constant of each spring to be tested and recorded alongside the spring rate.

Chapter 3.3 discusses the two different testing methods using a pulley system with a mass and string to apply torque to the spring. In the first test, the mass was dropped with the string near tension and the resultant spring response was recorded. New springs were manufactured for this test with constant outer diameter, inner diameter, and pitch. The springs were printed with variable spring leg width and spring thickness to determine the relationship between these two spring geometries and spring constants. Due to uncertainties involving the dropping of the mass, the spring data was cropped to start when the spring exhibited constant angular velocity. The data was also truncated at 1 second after the new starting point to keep the analysis of spring parameters within the same time scale as the desired walking gait of a quadruped robot. The cropped data was then modelled as a first order differential equation and spring parameters were calculated. The second test primarily focused on directly measuring the damping constant of the spring. The same pulley and mass set-up was used, and the mass was dropped from a known height. Spring rate was calculated from the final settling position of the spring after the mass was dropped, and the damping constant was calculated using conservation

of energy. Data from both tests were plotted to determine the relationship between spring geometry, spring rate, and damping constant. A new spring with arbitrary geometry was printed and tested to verify the experimental relationships developed for the spring parameters.

Finally, Chapter 3.4 discusses the design and evaluation of a second new hip joint to incorporate the new 3D printed hip spring into the quadruped robot hind leg. The dynamics of the new leg without a damper installed at the hip revealed an underdamped response at the hip. The desired overdamped behaviour of the scaled rat leg could then be achieved by adding a damper to the hip, making the new hip and hip spring designs viable solutions.

Chapter 2. Metal Spring

Background

The first approach taken in reducing the spring rate of the hip spring was to replace the existing metal spring. Following the manufacturing method of the previous hip spring, the new spring was made by hand winding ASTM A228 steel wire around a mandrel. The following equation was used to determine the wire diameter d, spring diameter D, and number of coils N required for the desired spring rate k.

$$k = \frac{d^4 E}{64DN} \tag{1}$$

To account for elastic deformation in the wire during the manufacturing, the mandrel diameter had to be smaller than the desired spring inner diameter. The mandrel diameter was calculated by extrapolating Table 23. Arbor Diameter for Springs Made from Music Wire in Machinery's Handbook 27th Edition [8]. The desired mandrel diameter was 34.923 mm, however a 1 in nominal pipe with an outer diameter of 33.401 mm was the closest to the desired value that could be achieved with available materials. The manufactured spring dimensions and parameters are listed in Table 2-1 along with the initially desired values.

Table 2-1: New Metal Spring Dimensions

	Wire diameter (mm | in)	Number of Active Coils	Mean Coil Diameter (mm)	Spring Rate (Nm/rad)
Desired Value	4.763 | 3/16	3.056	40	13.38
Actual Value	4.763 | 3/16	3.056	43	12.44

The hip joint was redesigned to accommodate the new spring and damper as shown in Figure 2. A pelvis that envelopes link 1 on both medial and lateral sides was developed to attach the new damper to the leg. Link 1 was enlarged to fit the new spring inside it. One of the spring legs was bent 90° out of plane to attach to the inside of the pelvis. Link 1 and link 2 were revised to have the same length ratio from the rat data.

One leg of the hip spring had to be bent 90° to insert into the pelvis piece. This was extremely difficult to do and the bend ended up in the wrong position. To compensate for this, a hole was drilled into the pelvis to attach the spring.

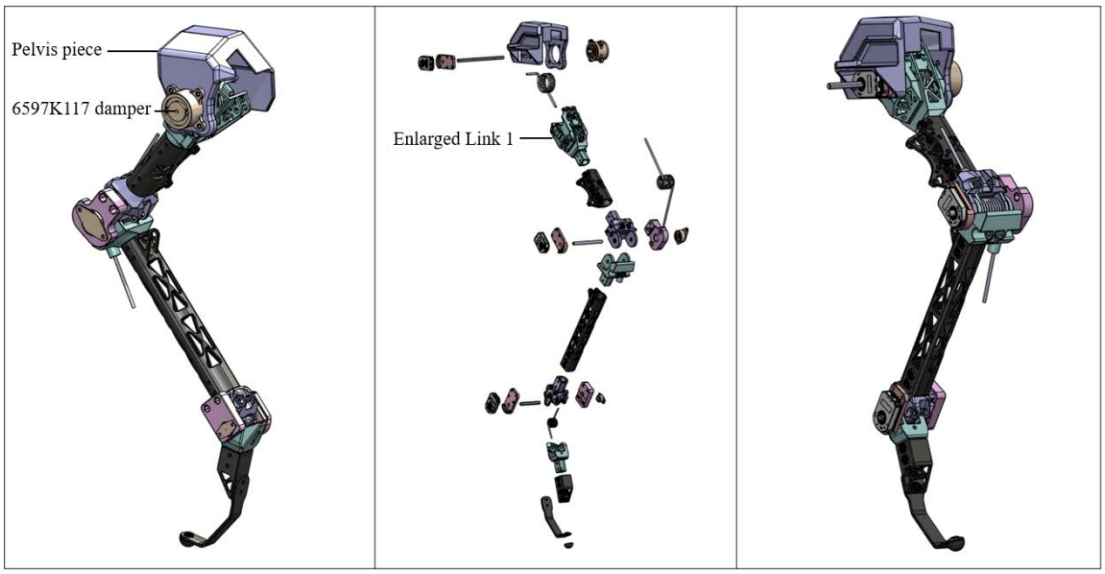

Figure 2: Quadruped robot hind leg with new hip spring and damper

2.1. Methods

A MATLAB app was created to help collect data from the quadruped robot leg that could be directly compared to the rat leg data. Encoder angles at the hip, knee, and ankle of the robot leg were read with an Arduino Due and communicated to MATLAB through the serial port. The app displayed the live readings of each joint angle and the text box display of each angle would turn green to serve as an indicator when the current angle was within 1° of the initial condition value for a selected rat leg test. Using the app as an aid, the robot leg was manually positioned to the same initial conditions as a rat leg test trial. The robot leg was then released, and the resultant angular deflection data was recorded through the app.

2.2. Results

Figure 3 below depicts the robot leg hip response plotted with the scaled rat leg data for one of the stimulated muscles. The response of both hip joints are similar in shape, however the robot leg settles at 107° whereas the rat leg settles at 102°.

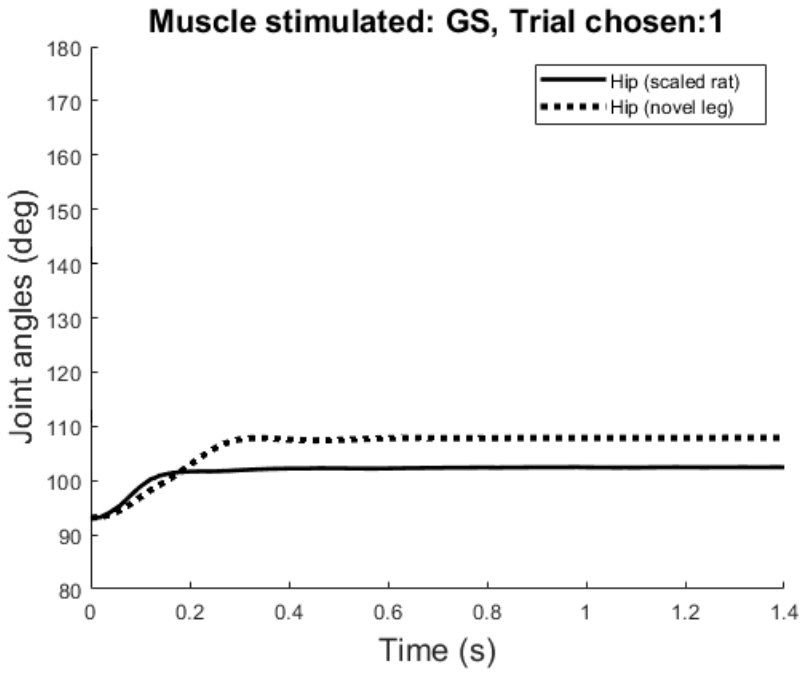

Figure 3: Quadruped robot hind leg and scaled rat hind leg passive response of the hip joint given same initial conditions

2.3. Discussion

The new quadruped leg exhibits biomimetic behavior with the new spring and damper pair, however the lack of fine control throughout the manufacturing process of the new hip spring resulted in an inaccurate steady state position. The data also suggested friction in the robot leg's knee joint that was not accounted for during modelling.

An improved manufacturing method and spring design was desired to create a better match between the passive dynamics of the quadruped hind leg and the scaled rat data. A 3D printed spring using Onyx was considered for the material's flexibility and toughness. 3D printing as a manufacturing method is also desirable for its high dimensional accuracy and accessibility to lab members who will work on future iterations of the quadruped robot. The AARL has 2 printers, the Onyx One and the Mark Two, capable of printing parts out of Onyx material with the Mark Two having the ability to print continuous fibers within the Onyx part.

Chapter 3. 3D Printed Spring

3.1. Background

A planar torsion spring design was chosen to replace the previous helical torsion spring as its geometry is better suited for 3D printing. Additionally, adjustability was desired in the new spring design to enable modifications of robot leg dynamics without disassembling the leg. Two approaches to adjustability were considered; a single spring with adjustable leg lengths, and a modular assembly that utilizes multiple non-adjustable springs in parallel to achieve the desired spring rate.

The spring with adjustable leg length, shown in Figure 4, was prototyped with 3D printed materials. A fully functional design would require the pink pin in Figure 4 to be manufactured out of metal to transmit the full force of the spring, especially with the high desired spring rate of the spring. This would decrease the ease and accessibility of manufacturing and maintaining the springs, making this approach less desirable. This design also heavily relied on alignment of the pin under cantilevered loads, adding potential jam and failure points. The added complexities of the adjustable leg length spring shifted focus away from it and towards an alternate design.

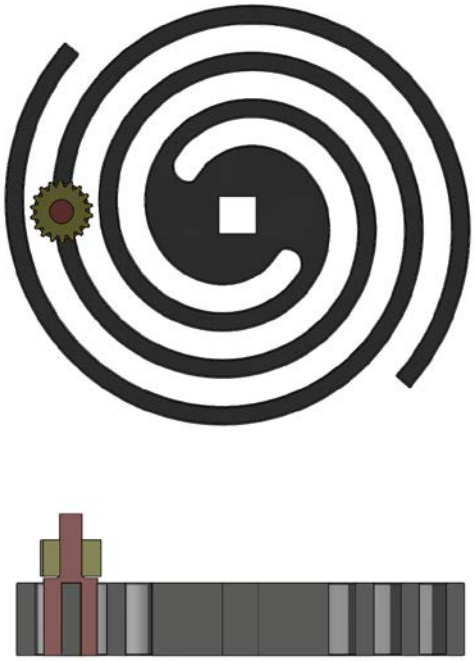

Figure 4: Prototype design of an adjustable torsion spring. The pink pin slides along the spring leg and locks in place using the yellow gear to adjust the effective spring leg length.

Instead of creating an adjustable spring, the spring rate of the hip joint can be made adjustable by allowing multiple springs to be attached in parallel. The overall spring rate of the hip would then be the sum of the spring rates that have been installed and could be adjusted by adding or removing springs. This design could be achieved without small moving parts, making it easier to maintain while also reducing the risk of failure. A relationship between geometry and spring rate needed to be developed for the 3D printed springs to make this design as efficient as possible.

The following equation can be used to calculate the spring rate of a flat spiral spring [9].

$$k = \frac{Ebh^3}{12L} \tag{2}$$

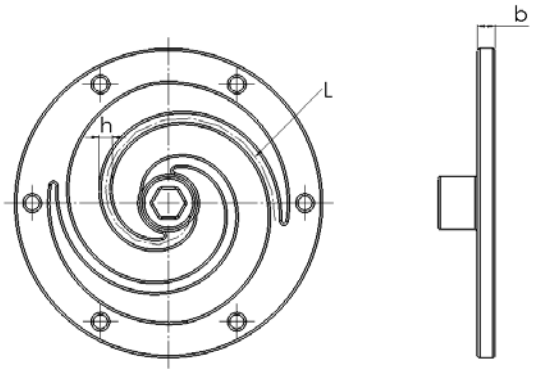

Figure 5: Planar torsion spring with labelled dimensions for calculating spring constant

In this formula L is the length of the spring leg, h is the spring leg width, and b is the spring thickness. This equation has been found to be applicable to springs with multiple revolutions but decreases in accuracy as the spiral revolution count of the spring decreases [9]. With a polymer as the material for the new spring, the Young's Modulus is low, therefore the spiral length will need to be minimized to achieve the high spring rate required at the hip. Ideally the hip will have a maximum of 2 springs: 1 spring with a spring rate close to the desired value, and an additional spring for adjustment if required. The new springs would then fall into the category of planar torsion springs that cannot be accurately defined by Eq (2). Finite element analysis (FEA) is a tool that can be used to obtain the spring rate of such a spring geometry manufactured from steel [9], but additional complexities from 3D printing make FEA less desirable.

Springs that are 3D printed have anisotropic material properties stemming from variations in printing parameters such as infill pattern, infill density, layer height, etc., which cannot be captured in Eq (2). Similarly, the performance of a 3D printed part is difficult to capture through FEA due to unknown material properties in areas of fusion between walls and layers. To avoid these known areas of uncertainty, an experimental relationship between spring geometry and spring rate was sought.

3.2. Preliminary Testing

The goal of preliminary testing was to determine whether a 3D printed spring could satisfy the requirements of the hip spring before continuing to develop a relationship between spring geometry and spring rate. The spring configurations tested in this section are listed in Table 3-1 below. Spring numbers (Spring No.) are used only in this section to cross reference between results tables. The spring geometry for P1 was chosen arbitrarily and tested for spring rate and range of motion. Spring P2 was then designed based on the results of P1 to get closer to the design criteria. This process was repeated until spring geometry P6.

Table 3-1: 3D printed spring geometries included in preliminary testing

Spring No.	OD (mm)	ID (mm)	Pitch (mm)	Legs	Leg Thickness (mm)	Spring Thickness (mm)	Infill Type
P1	44	14	19	2	4	5	37% Triangular
P2	54	14	33	2	6	4	37% Triangular
P3	54	14	20	4	3	6	37% Triangular
P4	54	14	20	3	4	4	37% Triangular
P5	54	14	20	2	5	12	37% Triangular
P6	54	14	20	2	5	12	100% Solid

Spring configuration P6 and other spring configurations introduced later in Chapter 3.3 are printed with 100% infill. It should be noted that this is a common infill pattern option provided by slicer software for 3D printed parts. Contrary to the name, parts printed with 100% infill still have small air gaps between walls and layers due to the nature of the 3D printing manufacturing process. For this paper, 100% infill is referencing the infill pattern option that will include small air gaps, not a fully solid part.

The spring configuration P1 was also tested with Kevlar and HSTS fiberglass. Figure 6 is a depiction of the continuous fiber (yellow) within the Onyx material (white).

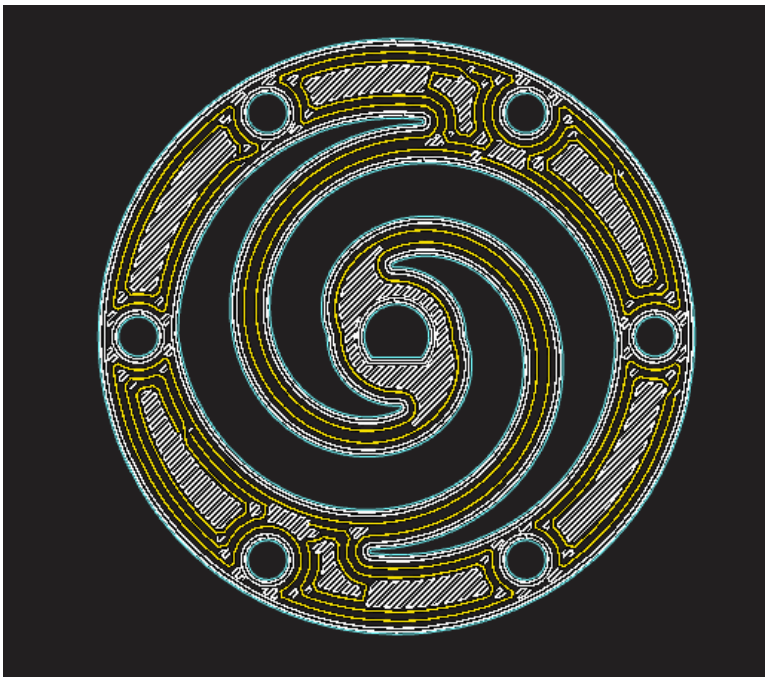

Figure 6: Continuous fiber within 3D printed Onyx spring

3.2.1. Methods

The testing set-up consisted of two 3D printed mounts bolted in-line to an MDF board, shown in Figure 7. Springs were bolted to one mount for testing, and an AMT103 encoder was press fit onto the other mount to record angular position. A D-profile shaft connects the encoder, spring, and a 3D printed lever arm. Weights were hung on the lever arm at $50, 75,$ and 100 mm from the axis of rotation in both clockwise and counterclockwise directions, and the resultant deflection was recorded. Bearings with 3D printed Onyx spacers were installed in the spring and encoder mounts to allow for smooth rotation of the shaft, and to fill the gap between the bearing inner diameter and shaft outer diameter.

The D-profile shaft used to connect the spring to the lever arm was replaced by a hex shaft due to high torque in the spring configurations P5 and P6 causing the shaft to the slip.

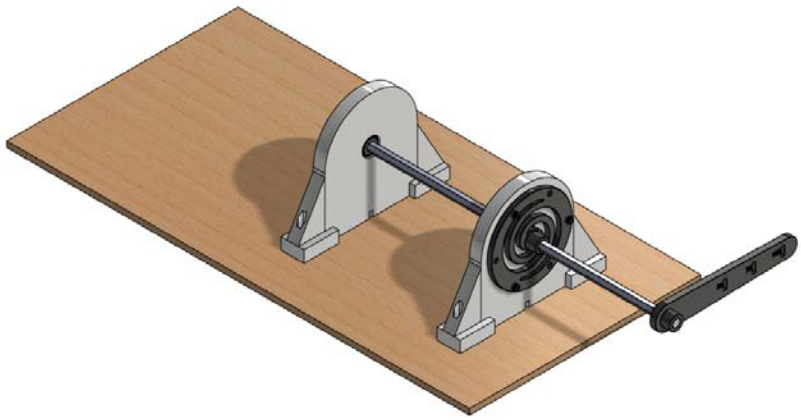

Figure 7: Model of experimental set up with lever arm

The range of motion for the 3D printed springs in this study is defined by the deflection of the spring until the spring legs contact another part of the spring. In clockwise deflection, the contact point was between the outer edge of the spring legs and the inner edge of the spring mounting ring, shown in blue in Figure 8. In counter-clockwise deflection, the contact point was between the inner and outer edges of the spring legs, shown in orange in Figure 8.

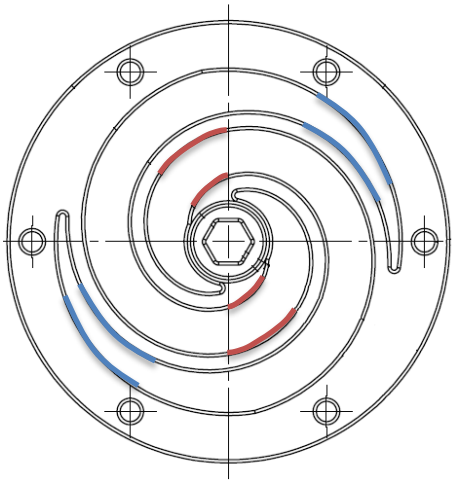

Figure 8: Self-contacting points on 3D printed spring

Deflection beyond these self-contact points was physically possible but would introduce non-linearities in spring behavior that are not considered for this study. To test for the range of motion, each spring was mounted on the test assembly and the pulley was manually twisted until self-contact was visible. The angular deflection at the point of contact was read by the encoder and printed to the serial monitor in Arduino.

3.2.2. Results

Below is a sample plot of applied torque versus angular deflection for spring P1.

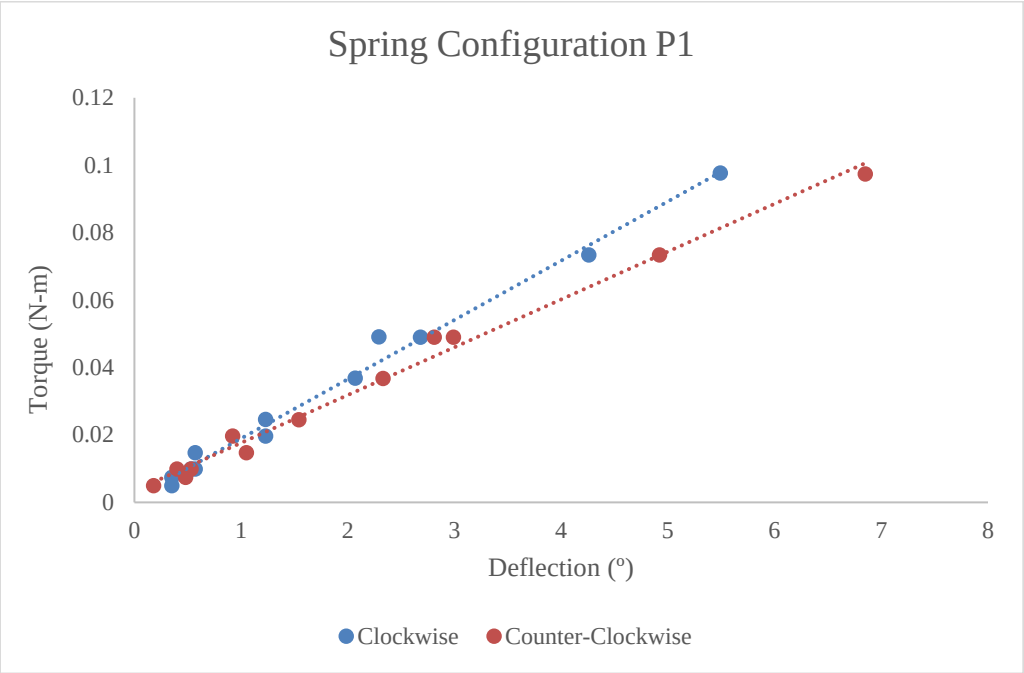

Figure 9: Experimental relationship between 3D printed spring deflection and applied torque in testing for spring configuration P1

All the tested spring configurations yielded plots similar to Figure *9* with linear relationships between applied torque and spring deflection. The slope of each data set can be taken as the experimental spring rate, which is tabulated below alongside range of motion for each spring configuration. A difference between clockwise and counter-clockwise deflection given the same torque input was observed across all spring configurations, therefore a clockwise and counter-clockwise spring rate was recorded for each spring.

Table 3-2: Range of Motion and Spring Rate of Preliminary Test Springs

Spring No.	Range of Motion (º)		Spring Rate (Nm/rad)	
	Clockwise	Counter-Clockwise	Clockwise	Counter-Clockwise
P1	60	56	1.104	0.888
P2	43	43	0.644	0.529
P3	33	35	0.920	0.716
P4	34	33	0.812	0.717
P5	43	36	4.932	5.561
P6	43	36	13.185	12.727

Springs printed with continuous fiber were tested in the same manner but presented separately in Table 3-3 to highlight the effect of the continuous fiber. Two separate trials were done with the spring with HSTS fiberglass due to audible cracking during the first test. The deflection in the spring when cracking occurred is unknown.

Table 3-3: Spring Rates of 3D Printed Springs with Continuous Fibers

Inlay Material	Concentric Fibers	Total Fiber Layers	Spring Rate (Nm/rad)	
			Clockwise	Counter-Clockwise
None	N/A	N/A	1.104	0.888
Kevlar	3	12	1.462	1.387
HSTS Fiberglass (trial 1)	2	8	3.627	3.592
HSTS Fiberglass (trial 2)	2	8	1.604	1.563

Printing with Kevlar continuous fiber increases the spring rate by over 50% in the counter-clockwise direction while an HSTS fiberglass continuous fiber increases the spring rate over 300%. The second trial with HSTS fiberglass showed a 76% increase in counter-clockwise spring rate over the spring with no continuous fiber.

3.2.3. Discussion

The preliminary test results verified that the desired spring rate and range of motion of the hip joint could be achieved with a 3D printed spring with spring configuration 2L5LT12ST100I. There is a distinction in spring rate dependent on the direction of the applied torque.

Printing with HSTS fiberglass continuous fiber drastically improves spring rate, however, the fiber broke when the spring was deflected to a certain point within its range of motion. It is notable that the spring rate with broken HSTS fiberglass is still higher than the spring rate with Kevlar. There were no indications of the Kevlar fibers breaking but this could not be confirmed.

While printing the preliminary springs, the Mark Two printer malfunctioned, producing visibly porous springs with low stiffness and high range of motion. A visual inspection indicated that P1, P5, and P6 were not affected by this issue, nor were the springs printed with continuous fibers. This issue was never resolved however and the Mark Two was decommissioned for the remainder of the project, preventing any additional testing of springs with continuous fibers.

The hip spring criteria was met, warranting the development of a relationship between spring geometry and spring rate for the modular hip design. The springs for the hip joint were set to have a constant outer diameter of 54 mm, an inner diameter of 14 mm, and a pitch of 20 mm to match spring 2L5LT12ST100I. The maximum spring leg

thickness and number of spring legs that allowed for the required range of motion was 5 mm and 2 respectively and were set to be the upper limits for further testing.

3.3. Experimental Spring Relationship

A relationship between spring geometry and spring rate is required for the modular hip design to be effective. If the spring rate of the hip needed to be increased, a new spring with a spring rate equal to the difference between current and desired spring rate could be printed. This could save hours of printing time as the other option is to print a new spring with a larger spring rate. Similarly, if the spring rate needed to be decreased, a combination of existing and new springs could be used. As more springs are printed, the AARL would build a catalogue of existing springs to choose from, increasing the range of spring rates that can be achieved without printing new springs.

With the spring parameter constraints identified during preliminary testing, springs with various geometries listed in Table 3-4 were printed to determine an experimental relationship between spring geometry and spring rate. Each spring configuration was printed with 37% triangular infill and 100% infill.

Table 3-4: Spring geometries tested for experimental spring rate relationship

Leg Thickness (mm)	Spring Thickness (mm)
2	4
3	4
4	4
5	2
5	4
5	8
5	12

Figure 10 below is an image of spring configuration 2L3LT4ST. The orientation depicted is how all springs are tested; clockwise applied torque results in the hex-shaft hole rotating clockwise as shown.

Figure 10: SolidWorks model of spring configuration 2L3LT4ST

Two tests were conducted to determine the spring rate of the springs. Both tests used the same set-up as the preliminary test but replaced the lever arm with a pulley, and replaced the D-profile shaft with a hex-shaft. A small or large pulley was used depending on the input torque desired. The small pulley was 3D printed out of PLA with a 20.39 mm radius. The large pulley was constructed from PETG, MDF board, and M3 bolts, with a 125 mm radius. Range of motion tests were again conducted on each spring.

3.3.1. Range of Motion

3.3.1.1.Results

The figures below show the relationship between spring geometry and range of motion in the clockwise and counter-clockwise direction.

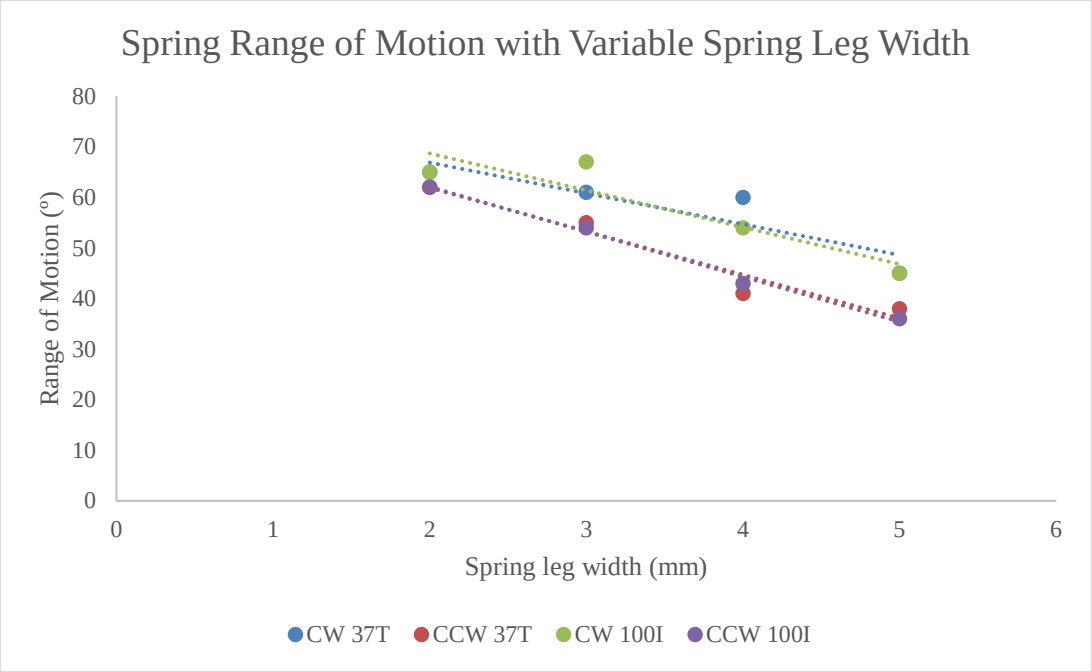

Figure 11: Range of motion of 3D printed springs with a constant spring thickness of 4 mm and variable spring leg width

From Figure 11, range of motion has an inverse relationship with increasing spring leg width. The springs consistently have more range of motion in the clockwise direction than counterclockwise. Range of motion in the clockwise direction decreases 6.7° per 1 mm increase in spring leg width. Range of motion in the counterclockwise direction decreases at a higher rate, 8.8° per 1 mm increase in spring leg width.

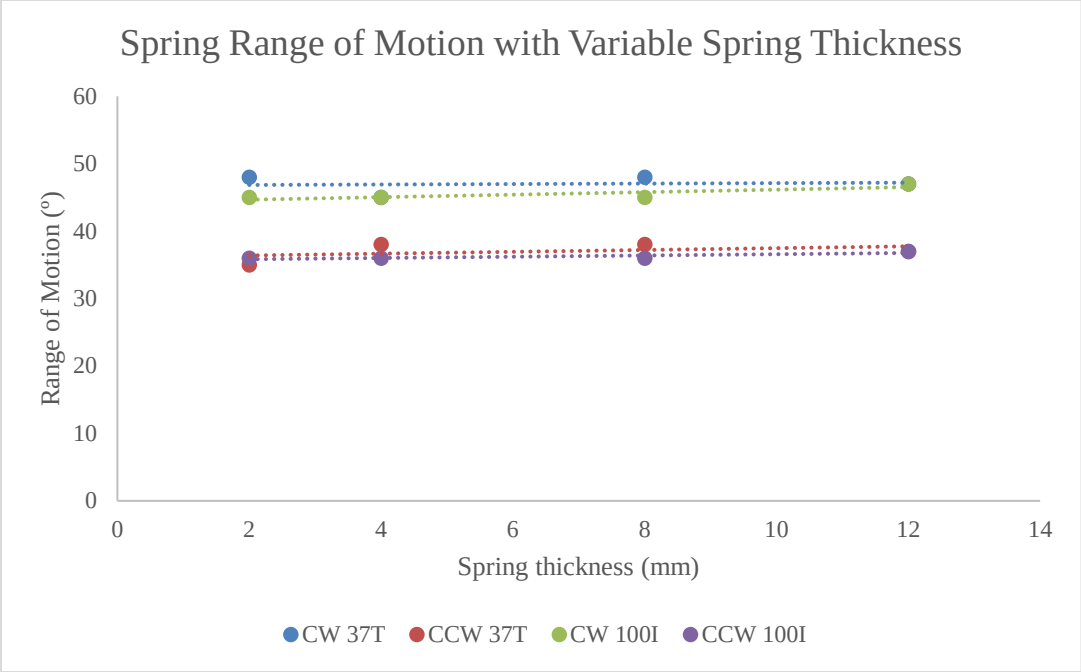

Figure 12: Range of motion of 3D printed springs with a constant spring leg width of 5 mm and variable spring thickness

From Figure 12, the range of motion remains constant as spring thickness changes. Range of motion in the clockwise direction is 10.6° greater than in the counterclockwise direction.

The springs' range of motion is unaffected by infill type but is affected by the direction of applied torque.

3.3.1.2.Discussion

As the spring leg width increases, there is less space for it to deflect before self-contacting, resulting in a reduced range of motion shown in Figure 11. Increasing the

spring thickness does not increase or decrease this space, therefore the same amount of room remains for the spring leg to deflect before self-contacting, resulting in a constant range of motion shown in Figure 12.

Both infill types have the same flexibility as neither factor into the springs' range of motion. The main differentiation in range of motion stems from the direction the spring is twisted. This is not an area of concern though as each spring configuration that was tested meets the full range of motion requirement of the quadruped robot hip.

3.3.2. Spring Parameters with First Order Response Modelling (Test 1)

Initially, spring rate was the sole spring parameter of interest. However, spring response data, such as the ones shown in Figure 13 and Figure 14, suggested there were significant damping properties in the springs that should be captured as well. To experimentally determine the spring rate and damping constant of the springs, the pulley system was first modelled as a second order system with a torque step input using the following equation:

$$(I + mr^2)\ddot{\theta} + b\dot{\theta} + k\theta = mgr \tag{3}$$

The inertia of the hex shaft and pulley were calculated by weighing each part, modelling the part in SolidWorks, and using the mass properties tab. This method assumed a uniform density throughout the part which resulted in some unknown error for the 3D printed parts due to uneven mass distribution from the infill. The error was negligible

when compared to the gravitational input force from the mass and deemed acceptable. A small pulley with an inertia of $6.17 \times 10^{-6}\ \mathrm{kg \cdot m^2}$ was used to test all springs except the springs with 12 mm spring thickness, which required a larger pulley to apply the desired torque. The larger pulley had an estimated inertia of $3.08\ \mathrm{kg \cdot m^2}$.

Various weights were hung from the pulley with a string and dropped with the string as close to tensioned as possible. The resultant angular deflection in the spring from the torque of the dropped mass was recorded by the encoder through MATLAB. Masses were chosen for each spring to maximize deflection during testing without self-contacting to capture spring behavior near maximum range of motion. Each spring was tested with 4 different masses. Each mass was used to apply clockwise and counterclockwise torques on the pulley, and each mass and direction combination had 4 recorded trials for a total of 32 data sets per spring.

The mass was stabilized from swinging laterally by hand post-drop, which affected the nature of the input. Dropping the mass by hand also may have changed in the input from a step to a ramp input if the mass was not released from all points of contact at the same time. To avoid the region of uncertainty in the system input, the response data was cropped to start once the angular velocity was constant. Given the negligible inertia provided by the small pulley, mass, and hex-shaft compared to the spring and damping properties, the system response was simplified to a first order system approximation with a step input for torque:

$$b\dot{\theta} + k\theta = mgr \tag{4}$$

The data used for system identification of the spring was further constrained to the first 1 second from the onset of constant angular velocity because the springs will be used in a dynamic system mimicking the walking stride of a medium sized dog with a walking stride of 0.75 seconds.

Spring rate k was calculated by taking the applied torque and dividing it by the deflection taken at the end of the constrained time. Damping constant was calculated using the following equation for a first order differential equation.

$$b = \frac{1}{3} t_s k \tag{5}$$

Here, t_s is the time it takes for the response to settle within 5% of the final value.

3.3.2.1.Results

Below are some sample plots of normalized single trial data with a simulated first order model of the spring calculated from the data.

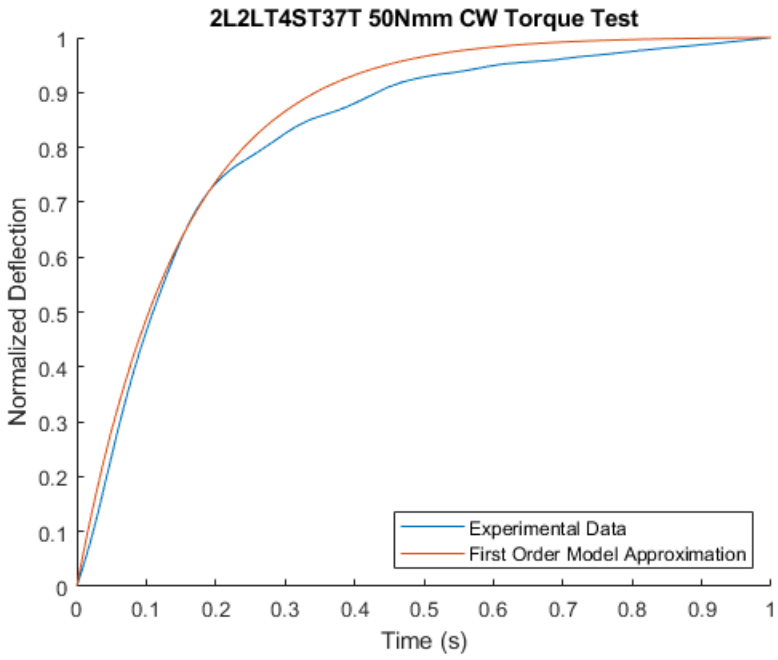

Figure 13: Normalized deflection data and simulated first order model of spring configuration 2L2LT4ST37T with an applied torque of 50 Nmm

The majority of simulated first order responses matched closely with the experimental data as shown in Figure 13. However, some trial data exhibited oscillations which could not be accurately simulated as a first order model as shown in Figure 14. For the trial data with oscillations, the first order model was able to capture the dominant damping behavior but further testing would be required to capture accurate damping characteristics.

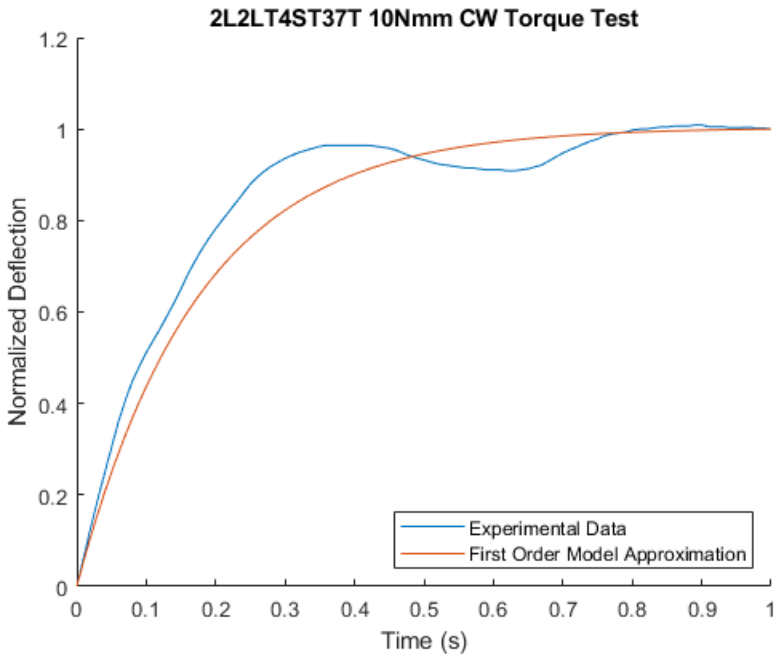

Figure 14: Normalized deflection data and simulated first order model of spring configuration 2L2LT4ST37T with an applied torque of 10 Nmm

The calculated spring constant and damping ratio from each trial is plotted for each spring. Below are the plots for the 2L2LT4ST37T spring.

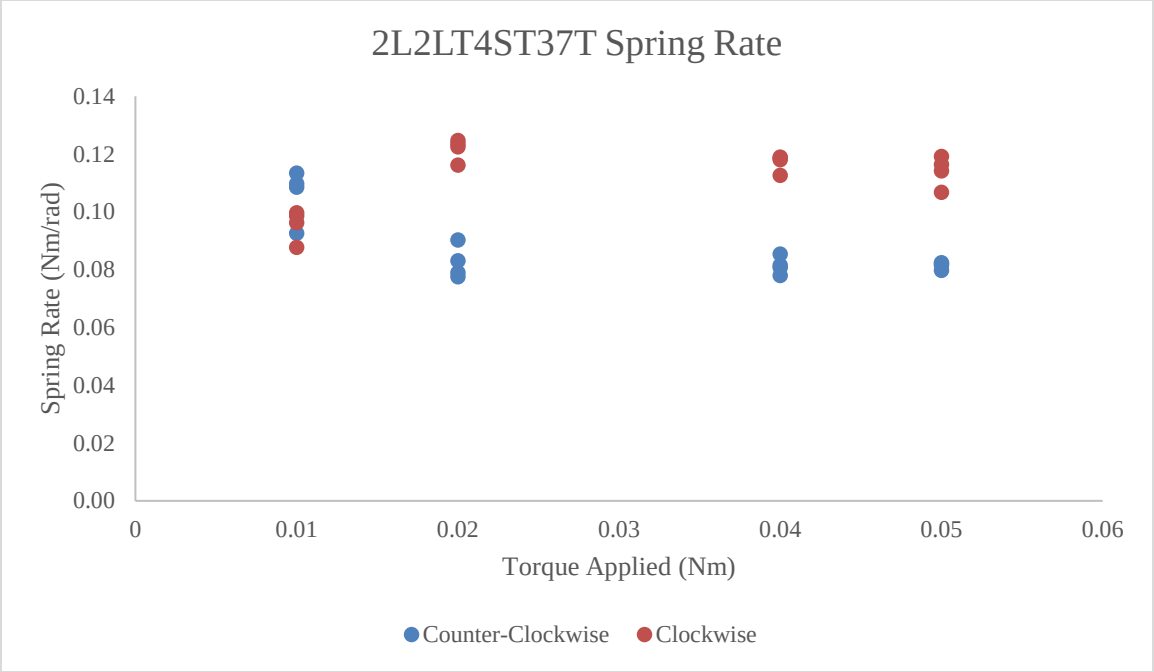

Figure 15: Experimental spring rates determined through first order system response modelling for spring configuration 2L2LT4ST37T

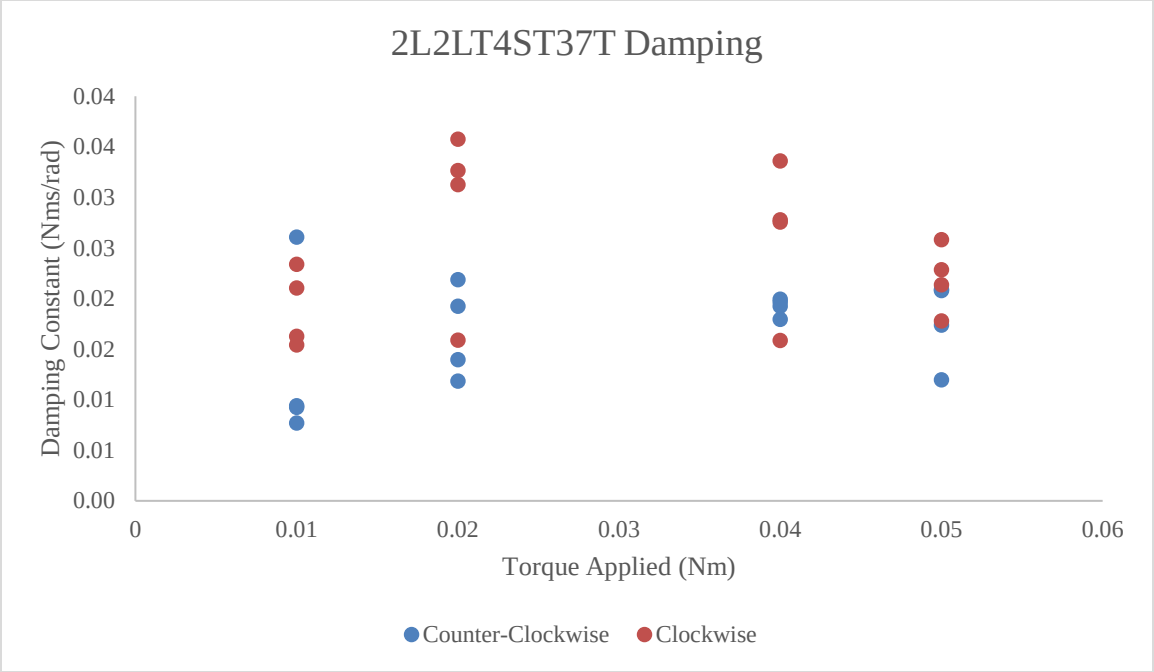

Figure 16: Experimental damping constants determined through first order system response modelling for spring configuration 2L2LT4ST37T

Spring rates appear to be constant except for the smallest applied torque (smallest deflection), therefore the average spring rate obtained from the largest applied torque is taken to be the overall spring rate of the spring and plotted below. Damping constants are more scattered without a clear trend. For simplified analysis, the overall damping constant of the spring is calculated in the same manner as the spring rate.

Data from the spring printed with 100% infill and 12 mm spring thickness was omitted from final analysis. A crack in the spring leg which reduced both its spring rate and damping properties was found after data collection for this test. A new spring was printed for test 2 in Section 3.3.3 and after the completion of test 2, a repeat of test 1 was

attempted to fill in the missing data in Figure 19 and Figure 20. The results of this test once again indicated there was a defect present in the spring and were discarded.

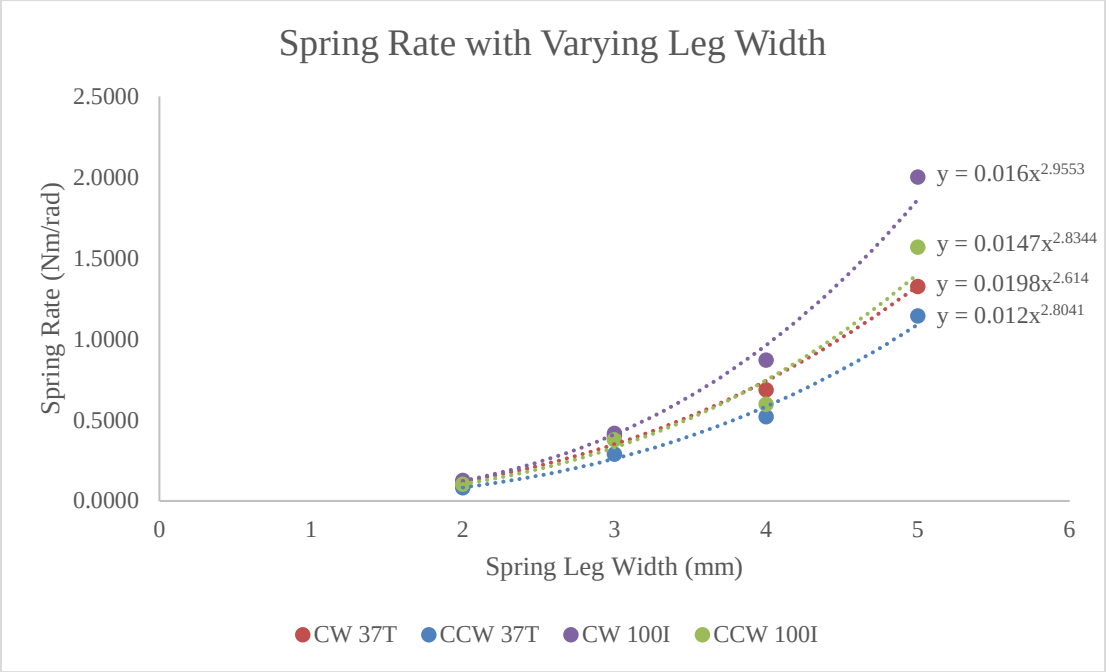

Figure 17: Experimental relationship between spring rate and 3D printed spring let width determined through first order system response modelling

The experimental relationship between spring rate and spring leg width matches closely with the relationship from Eq (2), where spring rate is proportional to spring leg width to the power of 3. For springs printed with either infill type, the spring rate is higher in the clockwise direction.

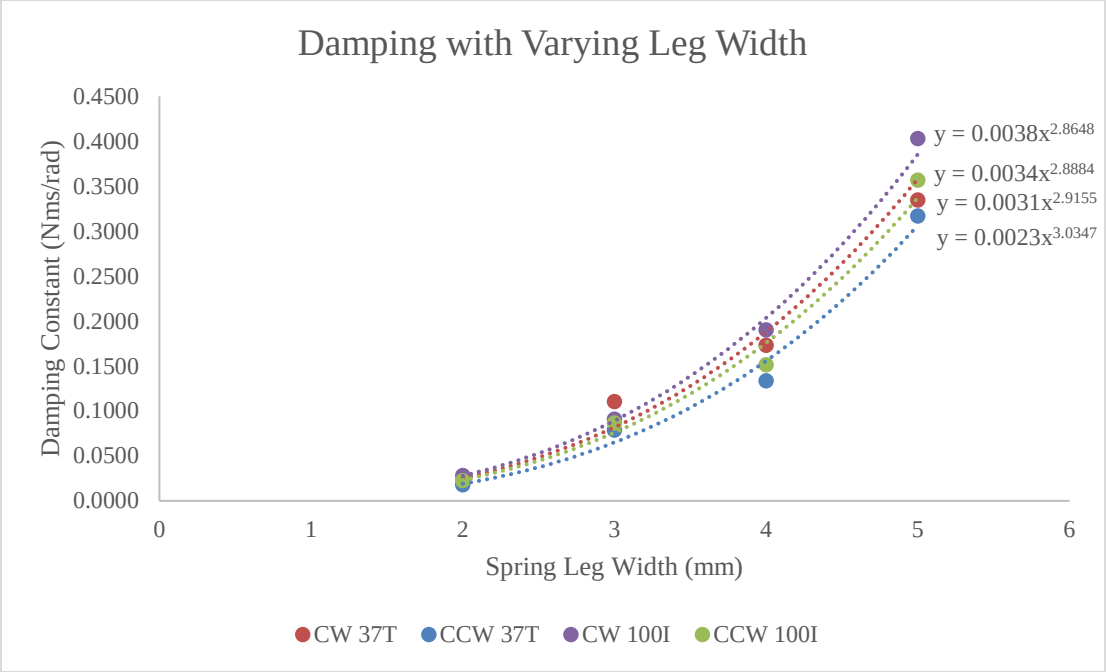

Figure 18: Experimental relationship between damping constant and 3D printed spring leg width determined through first order system response modelling

Similar to spring rate, spring damping exhibits a near cubic relationship to spring leg width. There is less distinction between springs printed with different infills in this data set.

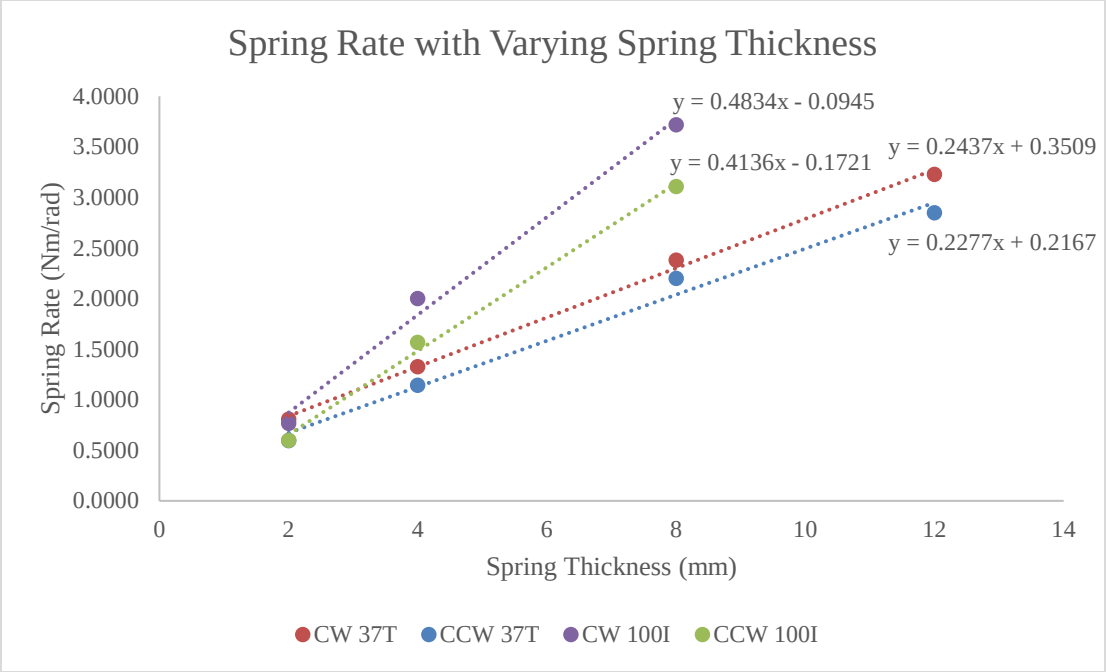

Figure 19: Experimental relationship between spring rate and 3D printed spring thickness determined through first order system response modelling

The experimental relationship between spring rate and spring thickness is linear, which is similar to the relationship from Eq (2). The experimental relationships also have a non-zero y intercepts.

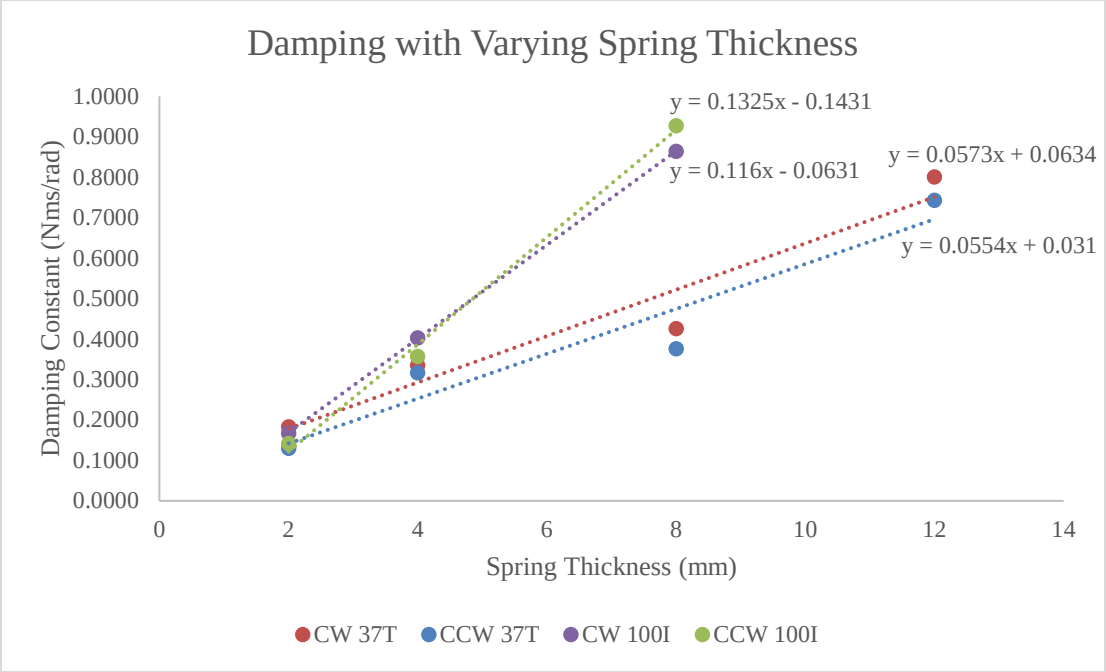

Figure 20: Experimental relationship between damping constant and 3D printed spring thickness determined through first order system response modelling

Damping also exhibits a linear relationship to spring thickness, although the relationship not as defined as the other data sets. There are also non-zero y intercepts for this relationship.

3.3.2.2.Discussion

Springs printed with 100% infill have more material in the spring legs to store strain energy and therefore have a higher spring rate than the springs printed with 37% triangular infill. Similarly, the ability to store more strain energy leads to higher damping in the 100% infill springs as well.

Overall, the spring rate relationship to spring leg width matches closely with Eq (2). The relationship between damping and spring leg width is similar to the relationship between spring rate and spring leg width. However, there is no equation to compare the experimental damping relationship against.

Spring rate has a linear experimental relationship with spring thickness like it does in Eq (2). For the springs printed with 37% triangular infill, the number of outer wall layers remains constant as the spring leg thickness increases, resulting in a slightly different stress distribution for each spring configuration. There are also pockets of air within the infill that do not contribute to spring rate. The springs printed with 100% infill have roughly double the increase in spring rate per unit change in spring thickness than the springs printed with 37% triangular infill. Contrary to its name though, 100% infill still has air gaps between layers and walls. Increasing the material density by eliminating the air gaps inside the spring legs results in an increase in spring rate. The non-zero y intercepts also indicate either calculation or modelling errors.

Most trial data sets resembled the system response in Figure 13 and could be modelled with a first order system with varying levels of accuracy. Some data sets exhibited oscillations while the overall deflection was still increasing, similar to Figure 14, indicating that the system was higher than second order. These could not be modelled accurately with a first order system, however the damping constant calculated with a first order system could be taken as an approximation of the dominant damping constant of the spring. Additional testing was desired to determine more accurate damping constants.

3.3.3. Spring Parameters with Conservation of Energy (Test 2)

This test was conducted to directly calculate the damping constant of the spring through conservation of energy. The governing equation for this test is shown below.

$$mgh_1 = mgh_2 + \frac{1}{2}mv^2 + \frac{1}{2}k\theta^2 + b\int \dot{\theta}^2 dt \quad (6)$$

Various weights were dropped with their geometric centers at a measured height h_1 while attached to the pulley with a string. The final height at the bottom of the drop h_2 was calculated by adding the arclength of the pulley at peak angular deflection, the distance from the attachment point of the mass to its geometric center, and the previously measured tensioned string length. The velocity v at peak deflection is 0, the peak deflection value θ is taken directly from the data, and the angular velocity $\dot{\theta}$ is calculated by taking the difference between adjacent angular deflection data points and dividing by the data time step. The limits of integration were 0 and the time of the first local maxima in the response data. Spring rate was again calculated by diving the applied torque by the steady state angular deflection. The damping coefficient was then found by rearranging Eq (6) and substituting in the known values.

Each spring was tested with 3 different masses. Each mass was used to apply clockwise and counterclockwise torques on the pulley, and each mass and direction combination had 4 recorded trials for a total of 24 data sets per spring.

Spring configurations 2L3LT4ST37T and 2L5LT12ST37T broke during testing and were also replaced. The results in Section 3.3.3.1 are taken from the replacement springs.

3.3.3.1. Results

Below is a sample plot of data from a single test trial for the spring configuration 2L2LT4ST100I.

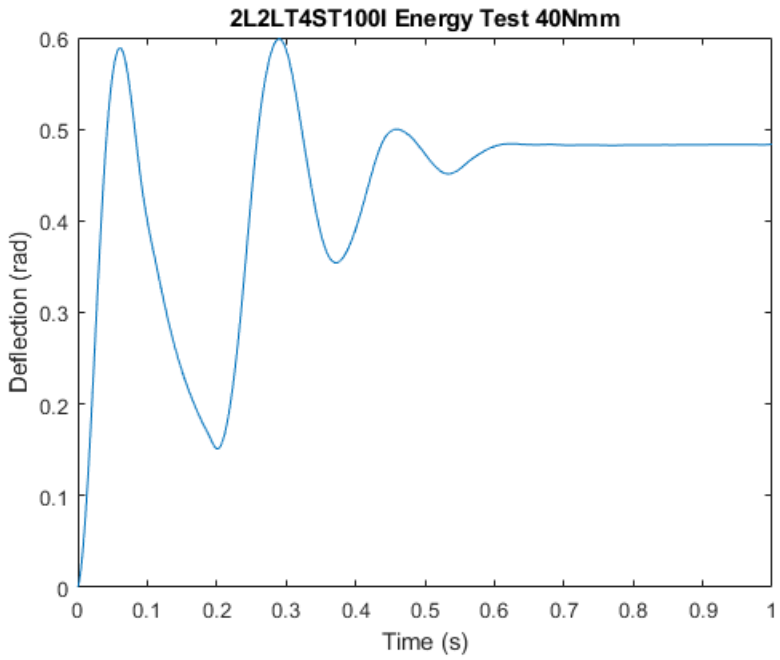

Figure 21: Conservation of energy test trial for spring configuration 2L2LT4ST100I with an applied torque of 40Nmm

The calculated spring constant and damping ratio from each trial are plotted for each spring. Below are the plots for the 2L2LT4ST100I spring.

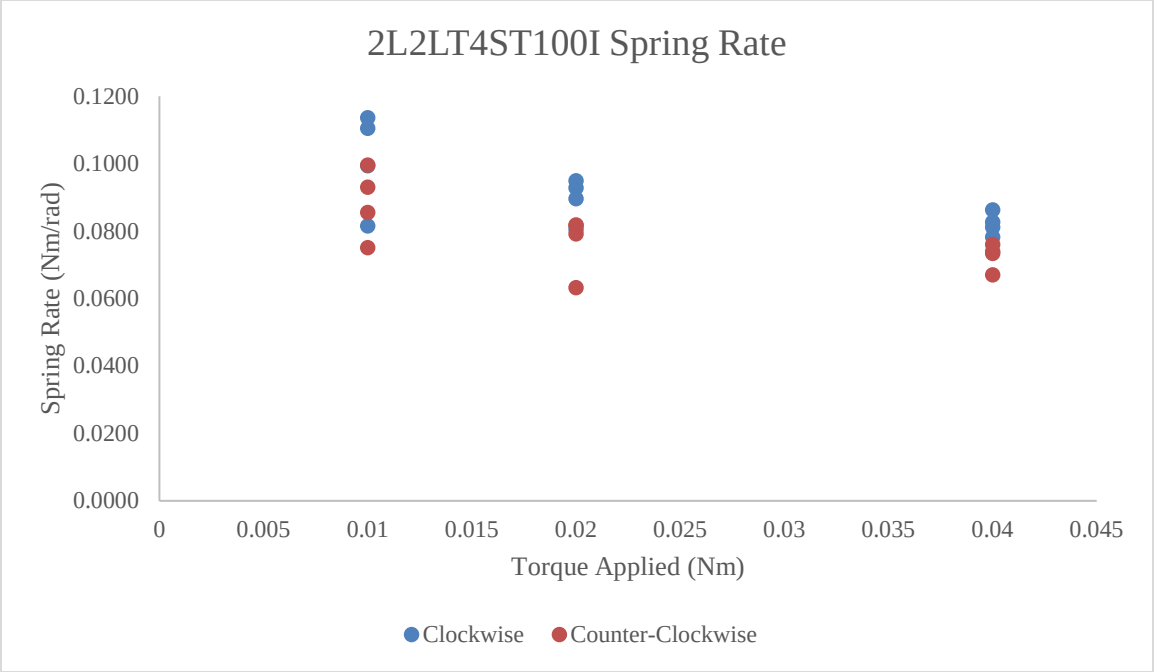

Figure 22: Experimental spring rates for spring configuration 2L2LT4ST100I determined through conservation of energy

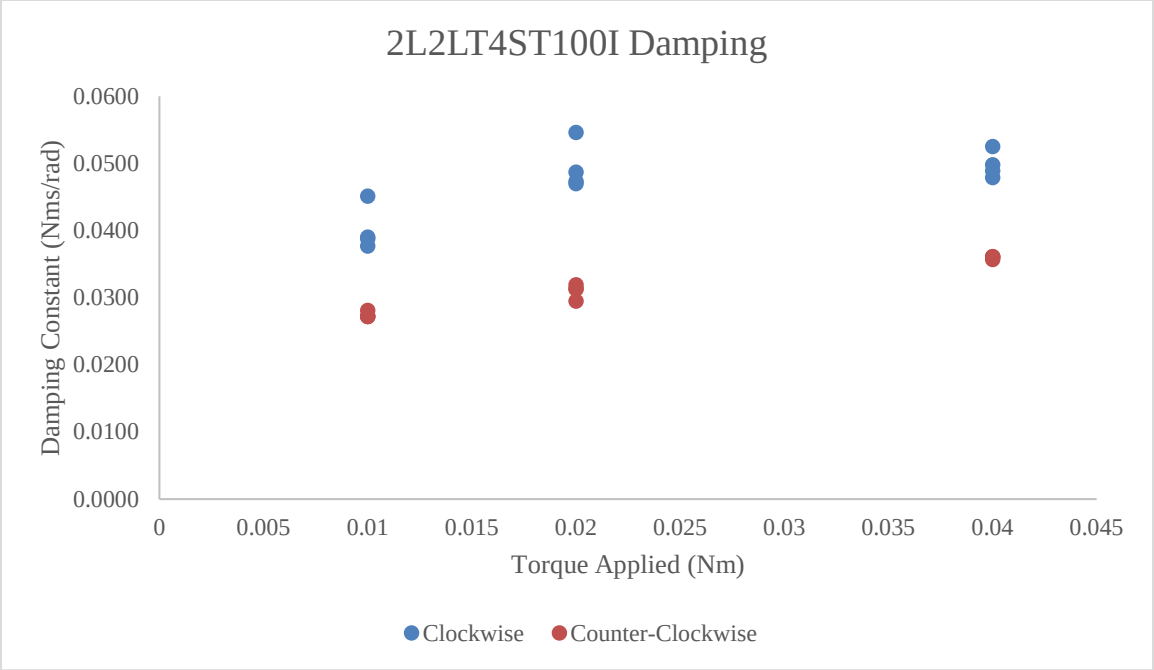

Figure 23: Experimental damping constants for spring configuration 2L2LT4ST100I determined through conservation of energy

Similar to test 1, spring rates converge to a final value as torque increases. The average spring rate obtained from the largest applied torque was taken to be the overall spring rate of the spring. The damping constant for the spring was also taken as the average of the experimental damping constants calculated from the largest applied torque. Overall spring rates and damping constants for spring configurations were plotted below.

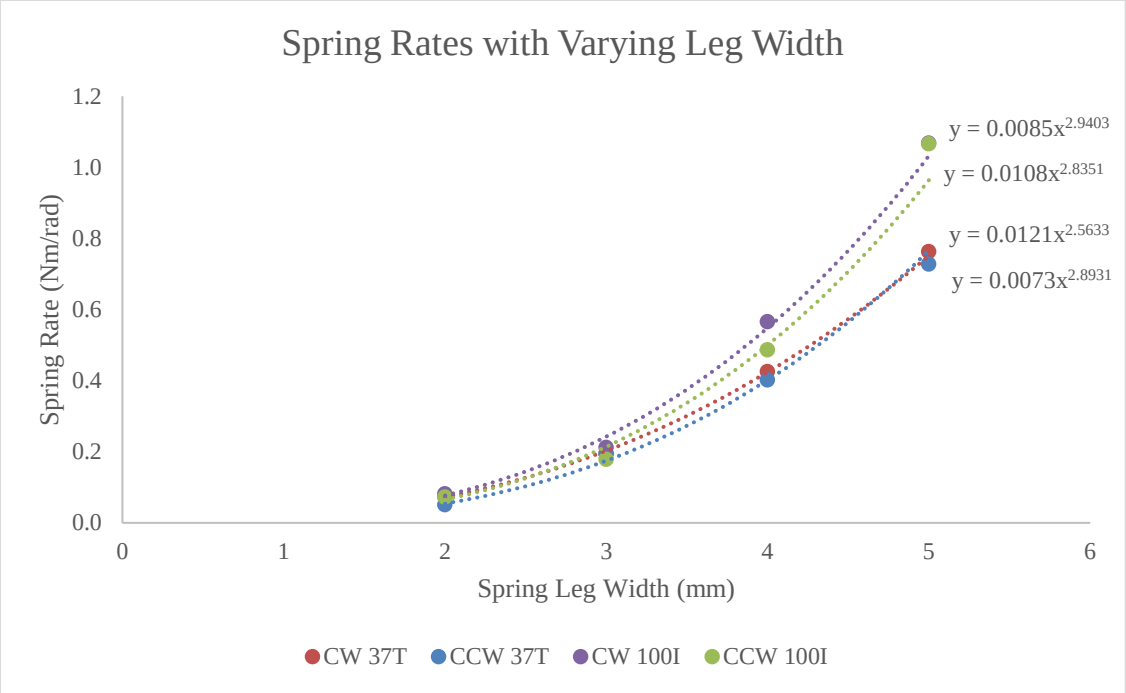

Figure 24: Experimental relationship between spring rate and 3D printed spring leg width determined through conservation of energy

The experimental relationship between spring rate and spring leg width is again close to the expected relationship from Eq (2) where spring rate is proportional to spring leg width cubed. There is a clear distinction in the spring rate between infill types.

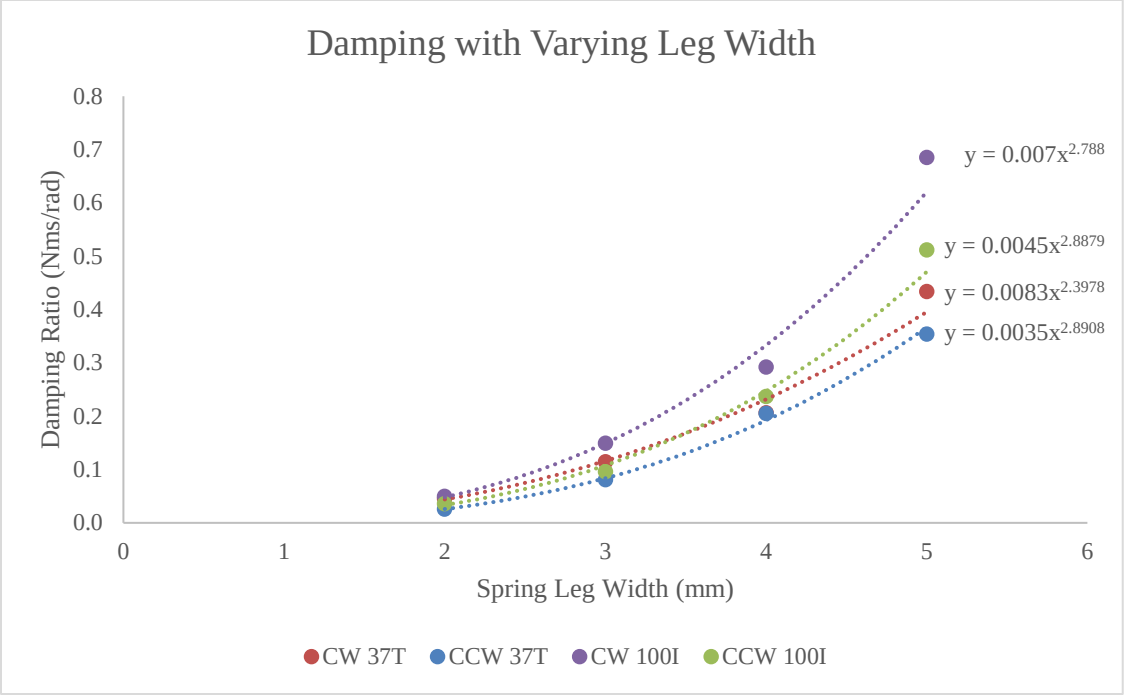

Figure 25: Experimental relationship between spring damping and 3D printed spring leg width determined through conservation of energy

The experimental relationship between damping constant and spring leg width is again best fit with a power function. The exponents are all near the expected value of 3, with the plot of clockwise damping constant for 37% triangular infill springs having the largest difference.

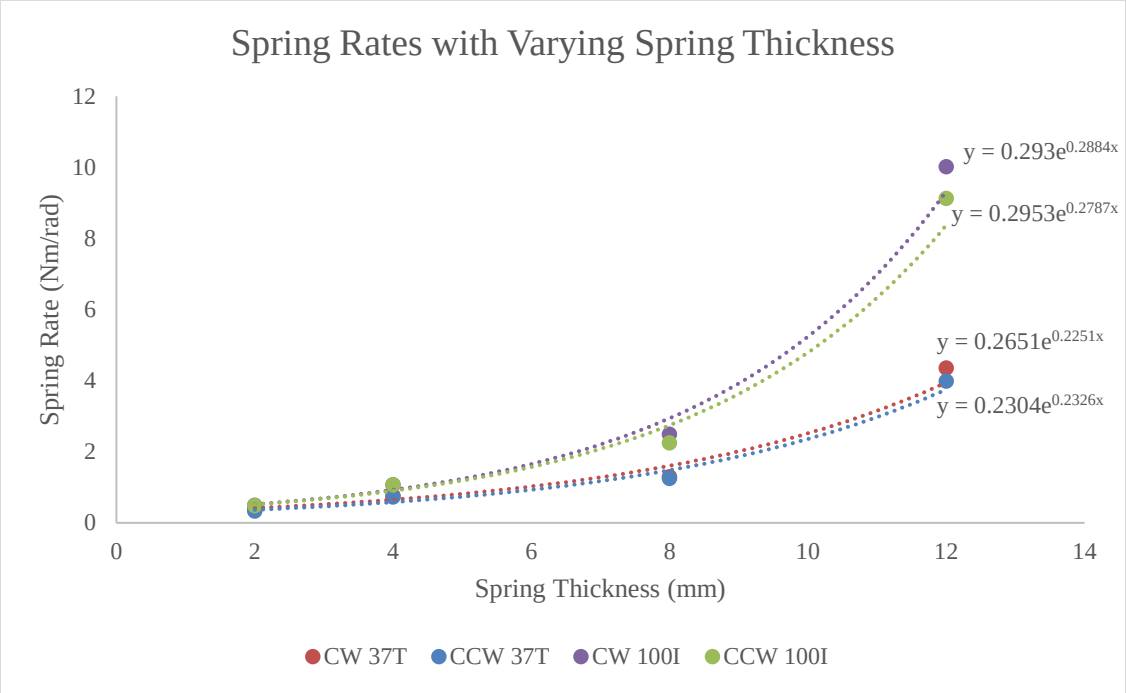

Figure 26: Experimental relationship between spring rate and 3D printed spring thickness determined through conservation of energy

The experimental relationship between spring rate and spring thickness is best fit with an exponential function, which contrasts the expected relationship from Eq (2) and the step input test where the spring rate is linearly proportional to spring thickness. The distinction in spring rate between the infill types is again prominent.

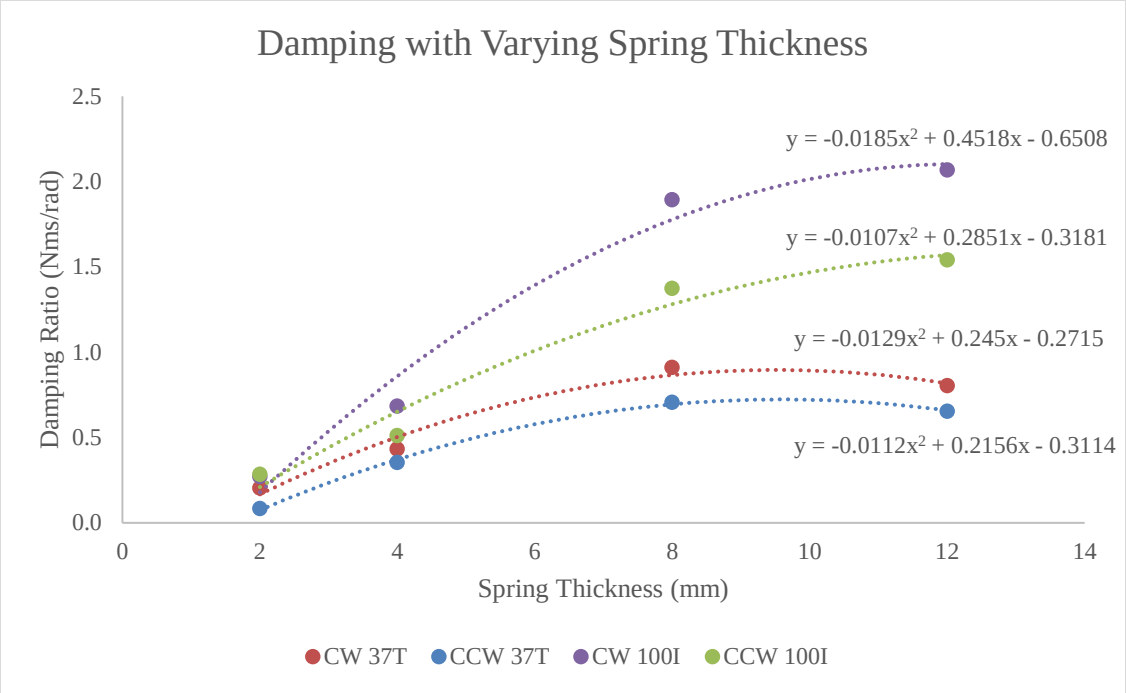

Figure 27: Experimental relationship between spring damping and 3D printed spring thickness determined through conservation of energy

The experimental relationship between damping constant and spring thickness was best fit with a negative quadratic function. The outliers in this data set are obtained from the 2 newly printed springs with 12 mm thickness.

For all tests, the springs printed with 100% infill exhibit higher spring rates and damping than the springs printed with 37% triangular infill.

3.3.3.2. Discussion

In general, the spring rates obtained from this testing method were slightly lower than those obtained from test 1, which was expected as there was a significant increase in

energy input leading to more deflection for the same test mass. The exceptions to this are the 2 new springs with 12 mm thickness. It is hypothesized that as the spring legs deflect, there is delamination occurring within the infill to allow for the deflection, which in turn decreases the spring rate in future tests. As spring leg thickness increases, the percentage volume of infill within the spring leg also increases. Lowered spring rate from infill delamination are then expected to be more prominent in springs with large leg thicknesses. Newly printed springs would not have such delamination prior to testing leading to higher spring rates. With more use near maximum deflection, it is expected that the spring rate of these springs would decrease.

In terms of Eq (6), the comparatively high spring rates of the 2 new springs would also decrease the amount of damping produced by the spring. As the spring rates decrease due to hypothesized delamination, the damping constant would increase. Although the experimental spring rate and damping constant relationships to spring thickness are hypothesized to change with additional testing, the relationships developed from this test will be used for comparison to first order modelling.

This experiment did not provide additional clarity into the relationship between spring geometry and spring damping. Damping constants determined in this test are roughly double their corresponding value from test 1. There is also no equation to compare the damping constants against to verify the experimental results. However, the AARL is currently designing an adjustable damper which could tune the robot leg response to mimic the rat leg response without knowing the exact damping constant of the spring. This is only possible if the damping provided by the spring is less than the

damping required to match the rat leg response. To test this, a new spring of configuration 2L5LT12ST100I was installed on the robot leg.

3.3.4. Quadruped Leg Response with Onyx Spring

A new hip joint was designed with a focus on bringing the hip spring attachment to the lateral side for easier access. Link 1 was reduced in size as it no longer needed to house the hip spring, and the pelvis was revised to incorporate a mounting point for the 3D printed springs. The new leg assembly is shown in Figure 29.

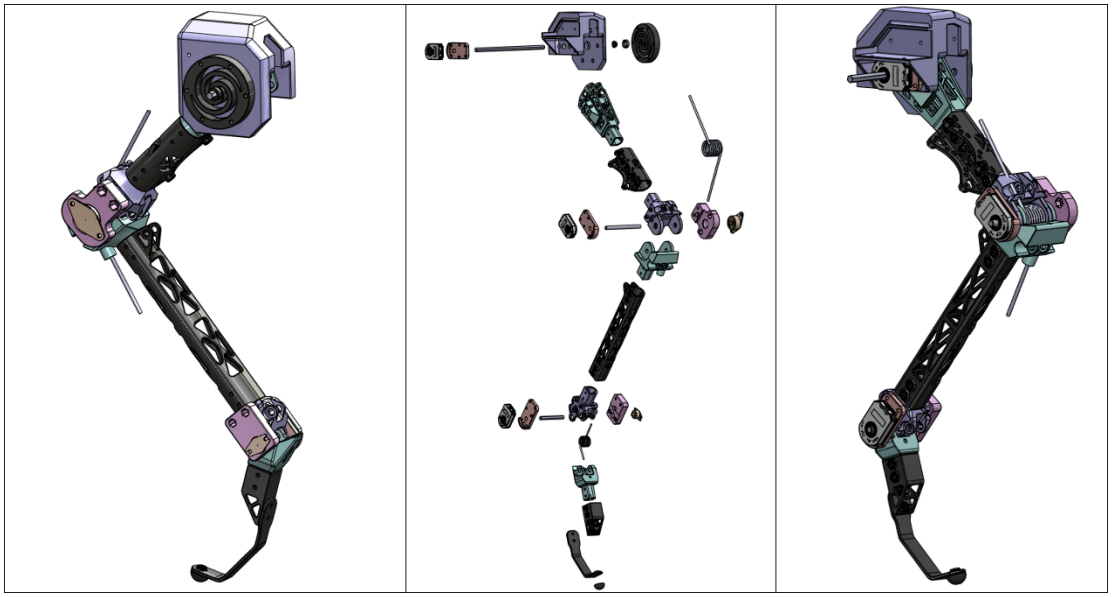

Figure 28: New quadruped robot hind leg with femur that allows for modular hip spring rate via 3D printed hip springs

The leg was manipulated to the desired initial conditions, and the passive response of the leg was collected following the procedure outlined in Section 2.1. There

was no rotary damper attached to the hip joint for this test, the sole source of damping torque was provided by the 3D printed hip spring. An optimizer script was then used to fit a spring and damping constant to the hip response.

3.3.4.1.Results

Data collected from the new hip with the 3D printed spring was plotted with the scaled rat leg data below. The robot hip exhibits an underdamped response. The settling position of the robot hip is very close to the rat hip. The spring and damping constants extracted from this hip response were 13.76 Nm/rad and 0.78 Nms/rad respectively.

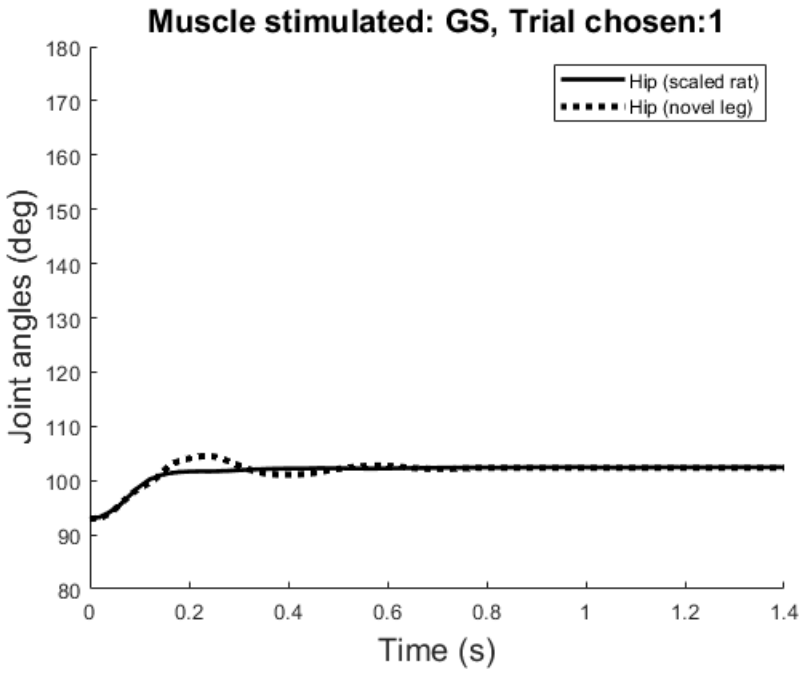

Figure 29: Quadruped robot hind leg and scaled rat hind leg passive response given same initial conditions

3.3.4.2.Discussion

The experimental spring rate in this test is higher than the desired spring rate, and the damping constant is lower than the 6597K117 damper, which results in the underdamped response in Figure 29. The small deflection in this test is hypothesized to cause the increase in spring rate over the previous tests. The underdamped nature of this response indicates that the addition of a damper could achieve the desired overdamped response and suggests that the 3D printed hip spring is viable for biomimetic passive dynamics.

3.4. Verification of Spring Parameter Relationships

A new spring configuration with 4.5 mm spring leg width and 6 mm spring thickness was printed to validate the spring parameter relationships that have been developed throughout this experiment. The same testing procedures of 3.3.2 and 3.3.3 were followed but only with 1 mass for each test; 1.5 kg for first order modelling, and 500 g for conservation of energy. Expected spring parameters for each testing method were determined by applying the relationships developed through prior testing to the difference in spring geometry between the new spring and a previously tested spring.

3.4.1. Results

Table 3-5: Experimental spring parameters for spring configuration 2L4.5LT6ST100I

First Order Modelling				
Torque Direction	Expected Spring Rate (Nm/rad)	Experimental Spring Rate (Nm/rad)	Expected Damping (Nms/rad)	Experimental Damping (Nms/rad)
CW	1.8479	1.8388	0.3994	0.2231
CCW	1.2512	1.4093	0.3189	0.1918

Conservation of Energy				
Torque Direction	Expected Spring Rate (Nm/rad)	Experimental Spring Rate (Nm/rad)	Expected Damping (Nms/rad)	Experimental Damping (Nms/rad)
CW	1.4252	1.1927	0.6574	0.8433
CCW	1.1865	1.0020	0.5150	0.6541

The errors in expected clockwise and counter-clockwise spring rates are 1% and 11% respectively using first order modelling. Conservation of energy calculation yields 20% and 18% errors in clockwise and counter-clockwise spring rates respectively. The error in damping constant is 79% and 66% in clockwise and counter-clockwise directions respectively using first order modelling, and 22% in both clockwise and counter-clockwise directions using conservation of energy calculation.

3.4.2. Discussion

The first order model relationship predicts the spring rate of the new spring well. The spring rate predicted using the conservation of energy relationship is less accurate, but for the purposes of improving biomimicry in the quadruped robot either method is

within an acceptable range of error. Experimental spring rate of spring configuration 2L4.5LT6ST100I determined through conservation of energy testing was significantly lower than first order model testing indicating a relationship between spring rate and type of input.

For predicting the damping constant, conservation of energy modelling was a much better than first order modelling, however the experimental damping constant in conservation of energy modelling is 3 times the experimental value in first order modelling, indicating that the spring's damping behavior is also dependent on the input. First order modelling overpredicted the damping constant which was expected as the derivation of its experimental relationships involved using overdamped representations of some of its test trials. Conservation of energy modelling underpredicted the experimental damping constant, but still had a higher expected damping constant than first order modelling.

More accurate spring characteristics, specifically damping constant, could have been determined by a frequency response. A frequency response would require a direct sinusoidal torque input and angular position readings as output. The AARL did not have access to a working torque control motor and did not have other projects that would benefit from a new torque control motor, so this approach was ultimately not pursued.

Chapter 4. Conclusions

4.1. Viability of 3D Printed Onyx Torsion Spring

As designed and manufactured in this experiment, a 3D printed torsion spring would be viable for biomimetic passive dynamics in the quadruped robot. The required spring rate and range of motion can be achieved, and the spring does not provide more damping than required to match the rat leg response. The addition of a damper could match the robot hip response to the rat leg response extremely well. Although the differences in clockwise and counter-clockwise spring performance are relatively small, this could be accounted for by installing 2 mirrored springs in parallel whose parameters sum to the desired values. This would result in equal spring performance in both directions.

The experimental relationships provided good estimates of spring rate based on changes in spring geometry. The estimates were within 20% of the tested value dependent on direction of applied torque and method of testing, which is acceptable for the purpose of improving biomimicry of a quadruped robot leg. Spring rate appears to be dependent on input type, with the step input used in first order modelling resulting in a higher spring rate. The mechanical inputs from the BPAs to the quadruped leg during locomotion are more similar to the step inputs used in first order model testing than the impacts of conservation of energy testing, however, from the results of this paper, the experimental relationships for spring rate developed through conservation of energy testing are recommended for estimating spring rates of newly manufactured spring

geometries. This is because spring configuration 2L5LT12ST100I was tested on the quadruped leg and determined to have a spring constant of 13.76 Nm/rad, and conservation of energy modelling predicted a spring rate of 9.33 Nm/rad which is closer than the 5.71 Nm/rad spring rate predicted by first order modelling. It is important to note that the equations of first order modelling were derived without data points for a spring printed with 12 mm geometry. Spring rates calculated from step inputs used in first order modelling were consistently higher than spring rates calculated from conservation of energy throughout this study, therefore it is hypothesized that an equation of first order modelling derived from data that included tests on a 12 mm thick spring would predict a higher spring rate than 9.33 Nm/rad and would be the recommended equation for estimating spring rate. However, until that hypothesis is confirmed, conservation of energy modelling equations in Figure 24 and Figure 26 are the better predictor of spring rate.

The experimental relationships developed to calculate damping constant through conservation of energy testing were more accurate than the experimental relationships developed through first order modelling, however like the spring rates, damping constant was also heavily dependent on input type. Due to the nature of the BPA inputs on the quadruped robot leg during locomotion, first order modelling equations in Figure 18 and Figure 20 are recommended for estimating damping constants of new spring geometries, even though it is expected to overpredict. This is because spring configuration 2L5LT12ST100I was demonstrated to have an underdamped response with a damping constant of 0.77 Nms/rad when tested on the quadruped leg. Conservation of energy

modelling predicted a damping constant of 2.11 Nms/rad for spring configuration 2L5LT12ST100I which is significantly higher than the experimental value. First order modelling overpredicts the damping constant for the same spring configuration at 1.44 Nms/rad, which is closer than conservation of energy modelling. With the knowledge that first order modelling can overpredict damping constant by nearly 100%, an emphasis is put on adjustability in the damper that will eventually be installed on the robot leg. Damping will need to be adjusted based on observational comparison of the robot leg response to the rat leg data.

Although 3D printed springs are viable in the tests conducted in this experiment, there are still concerns in the repeatability of the springs' performance. In the 12 mm thick springs specifically, 3 separate springs either had visible defects or showed behaviors that indicated defects after only 1 set of tests. These springs saw a reduction in spring rate of up to 75% of their expected value. It is unclear what the exact cause of these defects are as some springs withstood multiple tests and exhibited repeatable spring properties throughout. The springs that broke tended to have larger spring leg widths however, which leads to a recommended path forward in printing smaller leg widths with continuous fiber.

4.2. Future Work

First order modelling tests must be done for the spring geometries with 12 mm spring thickness in order to verify the appropriate modelling equations to use for

predicting spring rate and damping constant in new spring geometries. Lifecycle testing on all spring geometries is also recommended to determine when degradation in spring rate starts to occur.

A damper still needs to be installed on the hip joint to complete the passive dynamics of the robot leg. The hip joint will need to be modified again to include a mounting point for the damper, which can be designed once the damper design is finalized. 3D printed springs with reduced size could also be tested for future implementation on the knee and ankle joints.

Increasing the spring rate of the 3D printed torsion springs with continuous fiber should explored further, specifically springs with smaller leg widths. Preliminary testing showed that continuous fiber increases spring rate, while springs with smaller leg widths demonstrated greater repeatability in performance without breaking. If these two characteristics are additive in a spring, it could replace the hip spring while being less likely to break at any point in the legs range of motion.

If an alternative manufacturing method were to be considered, laser cutting with a metal base material would be a viable option. Laser cutting is not as immediately available as 3D printing to the AARL but would maintain high dimensional accuracy. Manufacturing a metal spring would result in a presumably more reliable part for the purposes of the quadruped robot and would also allow for the use of FEA to predict spring behavior.

Bibliography

[1] T. Buschmann, A. Ewald, A. von Twickel, and A. Büschges, “Controlling legs for locomotion—insights from robotics and neurobiology,” *Bioinspir. Biomim.*, vol. 10, no. 4, p. 041001, 2015, doi: 10.1088/1748-3190/10/4/041001.

[2] A. Hunt, M. Schmidt, M. Fischer, and R. Quinn, “A biologically based neural system coordinates the joints and legs of a tetrapod,” *Bioinspir. Biomim.*, vol. 10, no. 5, p. 055004, 2015, doi: 10.1088/1748-3190/10/5/055004.

[3] Gregory Sutton, Roger Quinn, Nicholas Szczecinski, and Hillel Chiel, “Neural control of rhythmic limb motion is shaped by size and speed”.

[4] M. H. Dickinson, C. T. Farley, R. J. Full, M. a. R. Koehl, R. Kram, and S. Lehman, “How Animals Move: An Integrative View,” *Science*, vol. 288, no. 5463, pp. 100–106, Apr. 2000, doi: 10.1126/science.288.5463.100.

[5] E. Krnacik, “Applying Biomimetic Passive Dynamics to a Quadruped Robot Leg,” Portland State University, 2022.

[6] W. T. Kano *et al.*, “Kinetic and temporospatial gait parameters in a heterogeneous group of dogs,” *BMC Veterinary Research*, vol. 12, no. 1, p. 2, Jan. 2016, doi: 10.1186/s12917-015-0631-2.

[7] “Onyx 3D Printer Filament and Printing Material | Markforged,” Markforged. Accessed: Apr. 25, 2024. [Online]. Available: https://markforged.com/materials/plastics/onyx

[8] E. Oberg, F. D. Jones, H. L. Horton, and H. H. Ryffel, “Spring Design,” in *Machinery’s Handbook*, 27th ed., New York, NY: Industrial Press, Inc., 2004.

[9] J. Liu *et al.*, “Stiffness estimation of planar spiral spring based on Gaussian process regression,” *Scientific Reports*, doi: 10.1038/s41598-022-15421-1.

[10] *FE Reference Handbook*, 10.0.1. NCEES, 2020.

Appendix A: CAD drawings of springs, damper, and joint pieces

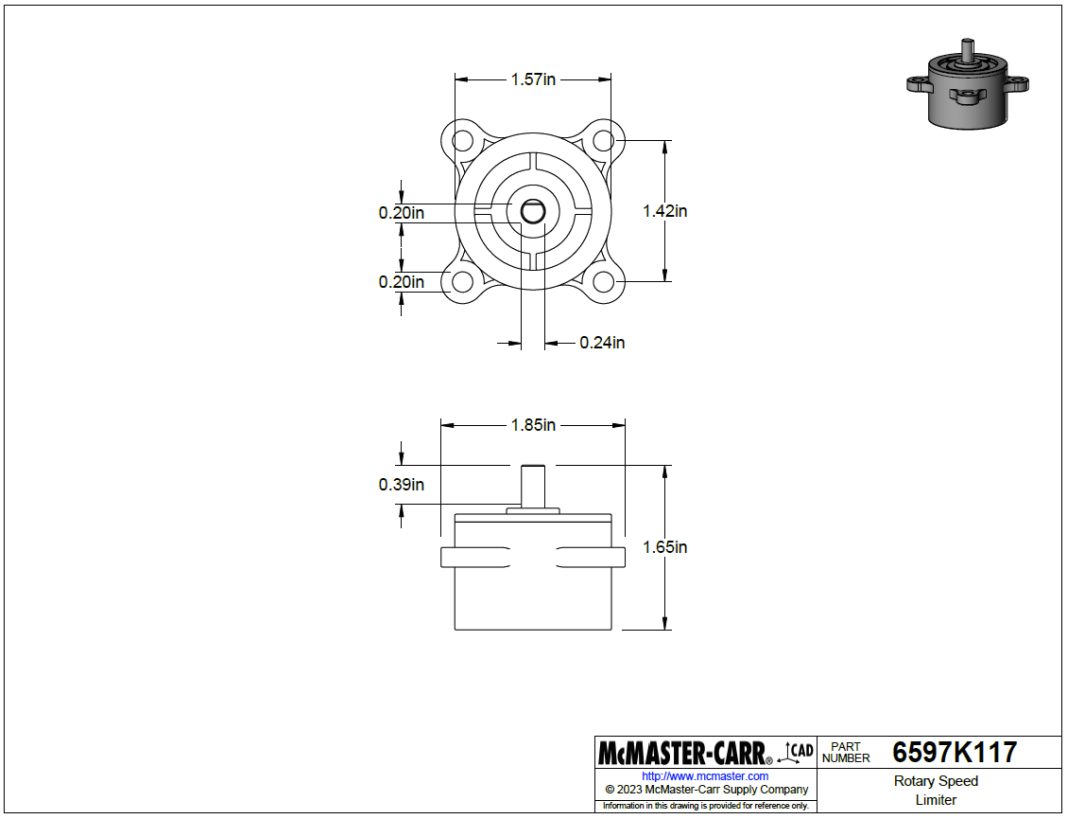

Figure A-1: CAD drawing of purchased 6597K117 damper from McMaster-Carr

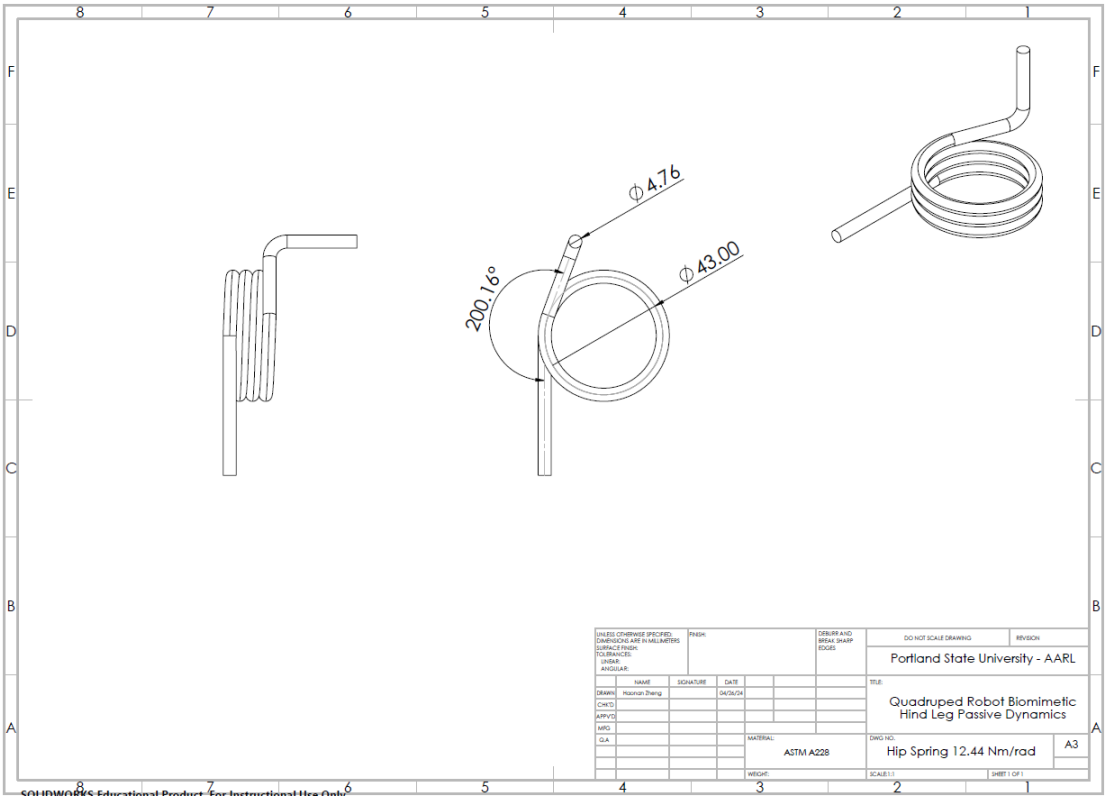

Figure A-2: CAD drawing of hand wound torsion spring with spring rate 12.44 Nm/rad

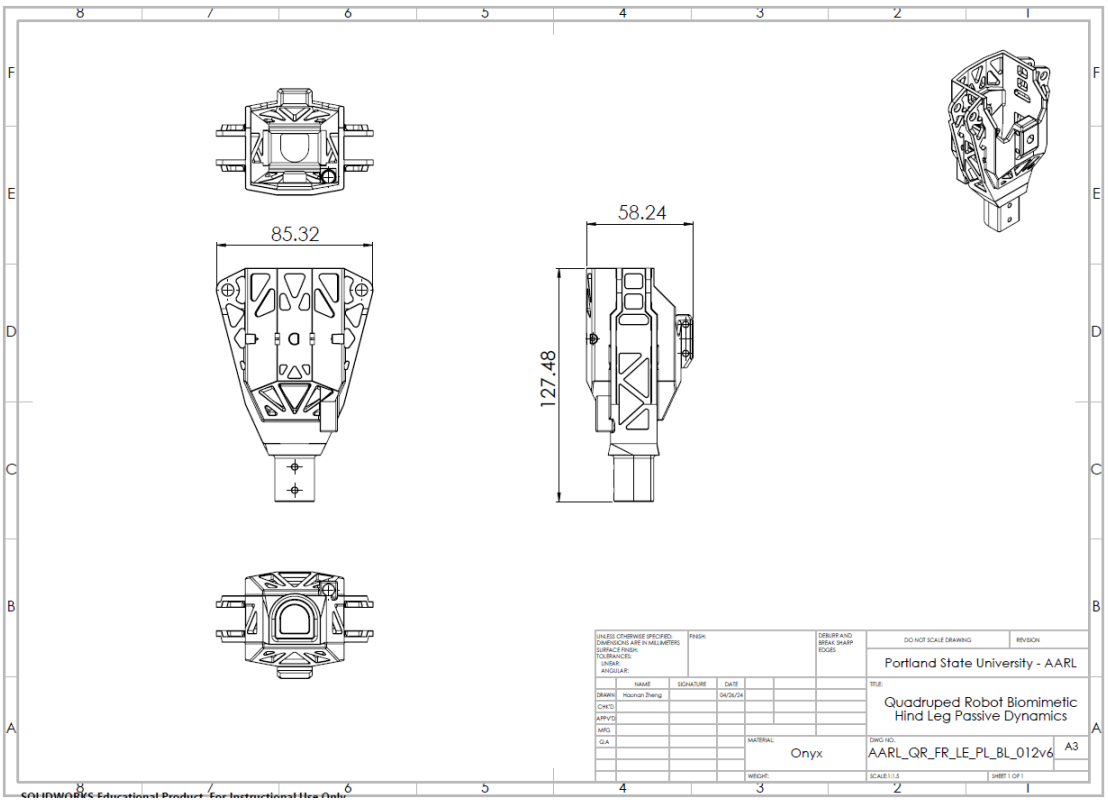

Figure A-3: CAD drawing of revised link 1 enlarged to house the new hand wound torsion hip spring

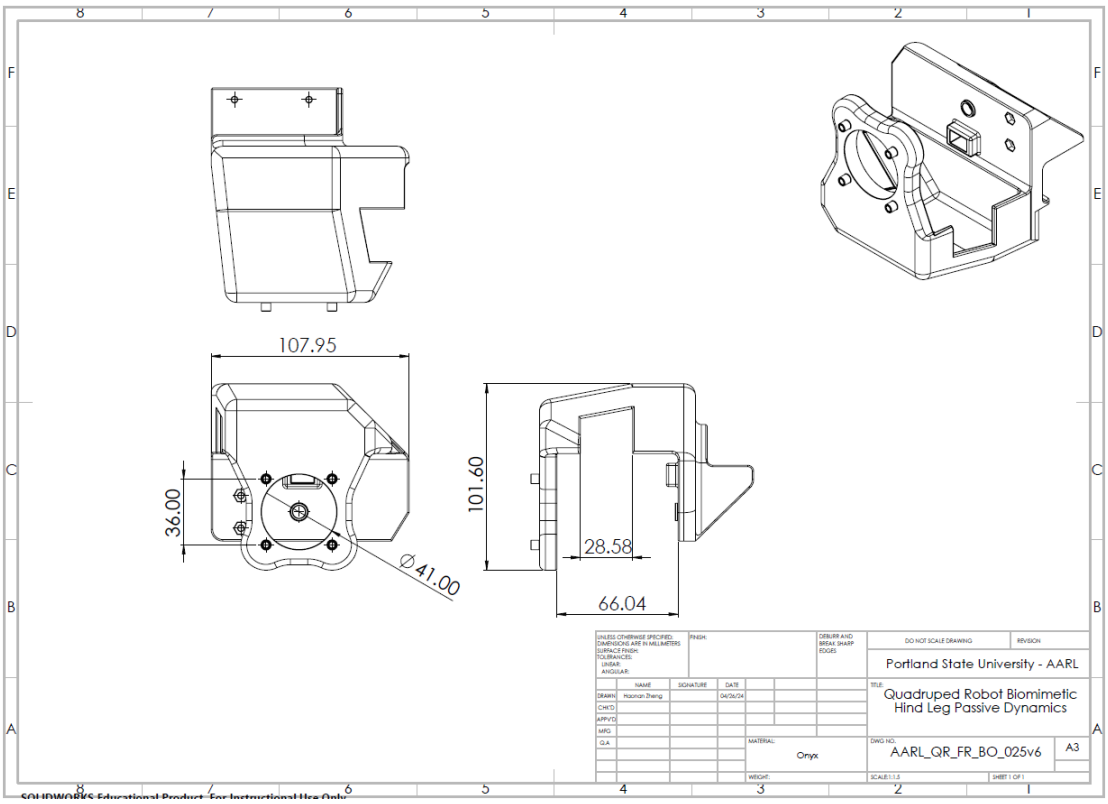

Figure A-4: CAD drawing of new pelvis piece designed to attach 6597K117damper to quadruped hip joint

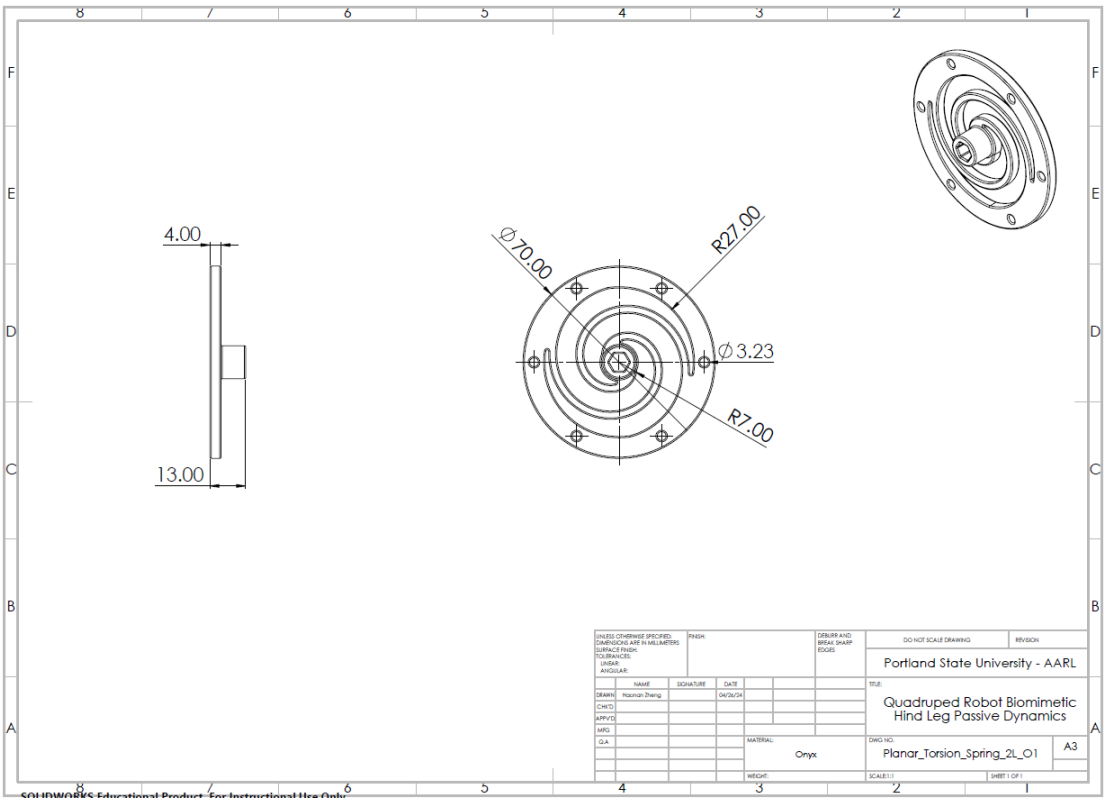

Figure A-5: 3D printed torsion spring configuration 2L2LT4ST

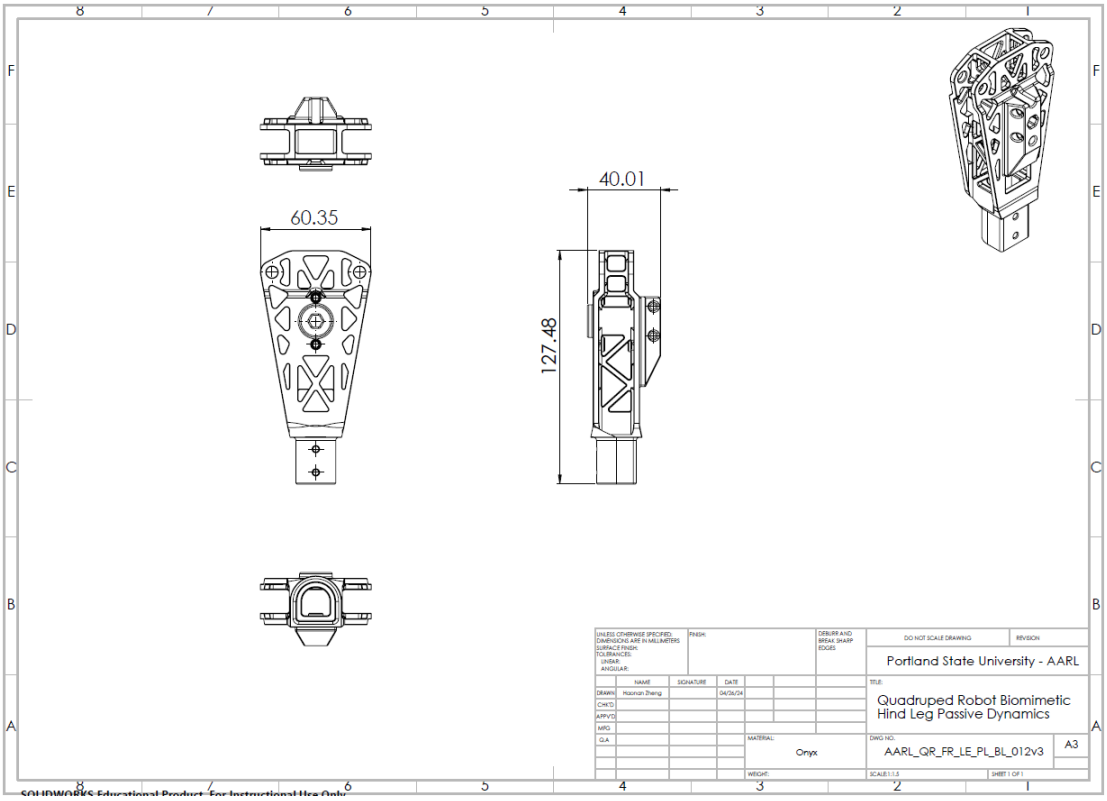

Figure A-6: CAD drawing of revised link 1 for 3D printed hip spring assembly

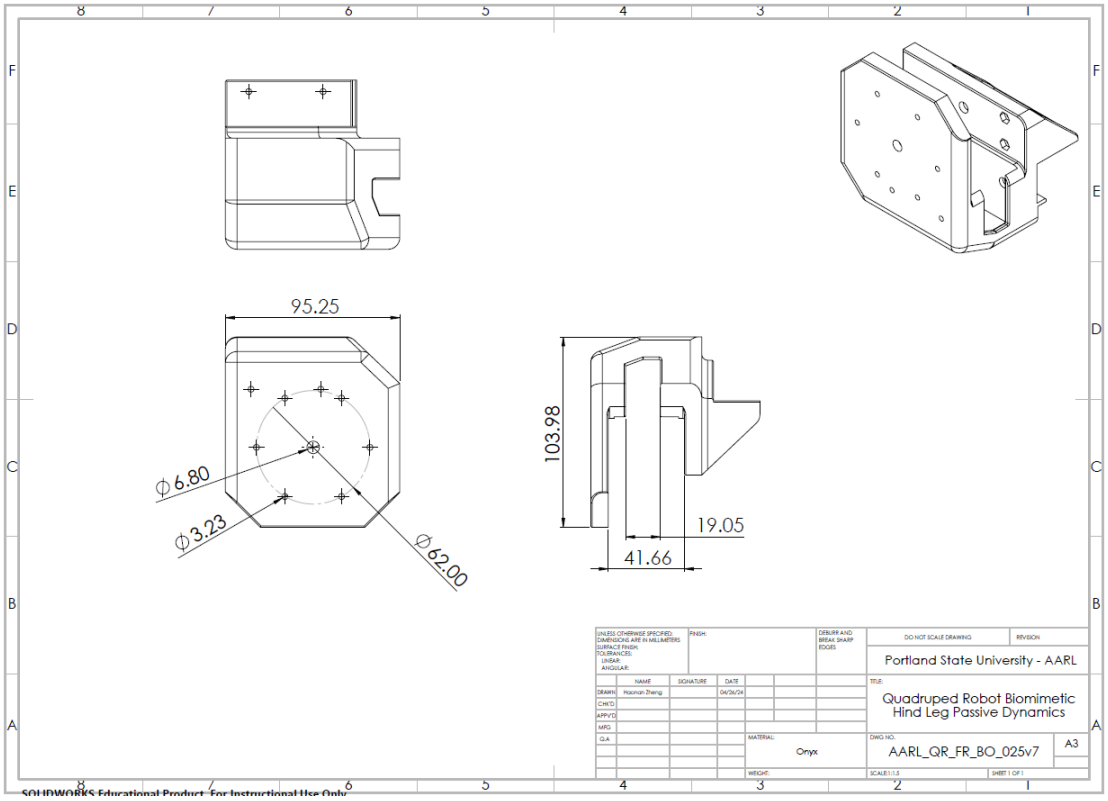

Figure A-7: CAD drawing of revised pelvis piece to accommodate new 3D printed springs

Appendix B: Spring Parameters – First Order System Modelling

Table B-1: Spring parameters calculated through first order system modelling for springs with 37% triangular infill and constant spring thickness

Fixed Spring Thickness 4mm 37T			
Spring Leg Width	**Direction**	**k (Nm/rad)**	**b (Nms/rad)**
2	CCW	0.0814	0.0178
	CW	0.1141	0.0219
3	CCW	0.2875	0.0786
	CW	0.4037	0.1103
4	CCW	0.5194	0.1334
	CW	0.6862	0.1729
5	CCW	1.1419	0.3169
	CW	1.3251	0.3344

Table B-2: Spring parameters calculated through first order system modelling for springs with 37% triangular infill and constant spring leg width

Fixed Spring Leg Width 5mm 37T			
Spring Thickness	**Direction**	**k (Nm/rad)**	**b (Nms/rad)**
2	CCW	0.5955	0.1301
	CW	0.8074	0.1830
4	CCW	1.1419	0.3169
	CW	1.3251	0.3344
8	CCW	2.2005	0.3756
	CW	2.3786	0.4255
12	CCW	2.8485	0.7427
	CW	3.2282	0.8003

Table B-3: Spring parameters calculated through first order system modelling for springs with 100% infill and constant spring thickness

Fixed Spring Thickness 4mm 100I			
Spring Leg Width	**Direction**	**k (Nm/rad)**	**b (Nms/rad)**
2	CCW	0.1025	0.0225
	CW	0.1264	0.0281
3	CCW	0.3775	0.0866
	CW	0.4170	0.0910
4	CCW	0.5974	0.1513
	CW	0.8698	0.1900
5	CCW	1.5670	0.3568
	CW	2.0000	0.4029

Table B-4: Spring parameters calculated through first order system modelling for springs with 100% infill and constant spring leg width

Fixed Spring Leg Width 5mm 100I			
Spring Thickness	**Direction**	**k (Nm/rad)**	**b (Nms/rad)**
2	CCW	0.5988	0.1419
	CW	0.7650	0.1674
4	CCW	1.5670	0.3568
	CW	2.0000	0.4029
8	CCW	3.1088	0.9269
	CW	3.7188	0.8640
12	CCW	3.0562	0.8855
	CW	3.1179	0.9218

Table B-5: Spring parameters calculated through first order system modelling

First Order System Modelling - 2L2LT4ST37T									
Applied Torque (Nm)		0.01		0.02		0.04		0.05	
Direction		CCW	CW	CCW	CW	CCW	CW	CCW	CW
k (Nm/rad)	trial 1	0.110	0.096	0.090	0.123	0.082	0.113	0.082	0.107
	trial 2	0.108	0.088	0.078	0.116	0.081	0.119	0.082	0.119
	trial 3	0.093	0.099	0.079	0.123	0.085	0.118	0.080	0.116
	trial 4	0.113	0.100	0.083	0.125	0.078	0.119	0.081	0.114
	average	**0.106**	**0.096**	**0.082**	**0.122**	**0.081**	**0.117**	**0.081**	**0.114**
b (Nms/rad)	trial 1	0.008	0.015	0.019	0.033	0.018	0.028	0.021	0.018
	trial 2	0.009	0.023	0.014	0.016	0.020	0.034	0.021	0.026
	trial 3	0.009	0.021	0.012	0.031	0.020	0.028	0.012	0.021
	trial 4	0.026	0.016	0.022	0.036	0.019	0.016	0.017	0.023
	average	**0.013**	**0.019**	**0.017**	**0.029**	**0.019**	**0.026**	**0.018**	**0.022**

First Order System Modelling - 2L2LT4ST100I									
Applied Torque (Nm)		0.02		0.03		0.05		0.06	
Direction		CCW	CW	CCW	CW	CCW	CW	CCW	CW
k (Nm/rad)	trial 1	0.136	0.173	0.126	0.149	0.114	0.140	0.101	0.137
	trial 2	0.141	0.137	0.128	0.149	0.116	0.122	0.103	0.130
	trial 3	0.141	0.129	0.141	0.148	0.130	0.120	0.100	0.120
	trial 4	0.133	0.161	0.136	0.141	0.111	0.134	0.106	0.118
	average	**0.138**	**0.150**	**0.133**	**0.147**	**0.118**	**0.129**	**0.103**	**0.126**
b (Nms/rad)	trial 1	0.035	0.033	0.010	0.026	0.026	0.030	0.020	0.031
	trial 2	0.030	0.037	0.030	0.026	0.026	0.027	0.024	0.028
	trial 3	0.033	0.022	0.030	0.035	0.031	0.025	0.021	0.026
	trial 4	0.027	0.036	0.028	0.029	0.023	0.029	0.024	0.028
	average	**0.031**	**0.032**	**0.024**	**0.029**	**0.026**	**0.028**	**0.022**	**0.028**

First Order System Modelling - 2L3LT4ST37T									
Applied Torque (Nm)		0.02		0.04		0.10		0.20	
Direction		CCW	CW	CCW	CW	CCW	CW	CCW	CW
k (Nm/rad)	trial 1	0.525	0.440	0.619	0.504	0.391	0.466	0.281	0.409
	trial 2	0.622	0.446	0.516	0.567	0.385	0.450	0.299	0.406
	trial 3	0.666	0.467	0.455	0.465	0.393	0.439	0.283	0.413
	trial 4	0.550	0.439	0.538	0.458	0.405	0.464	0.287	0.387
	average	**0.591**	**0.448**	**0.532**	**0.498**	**0.393**	**0.455**	**0.287**	**0.404**
b (Nms/rad)	trial 1	0.107	0.078	0.180	0.146	0.104	0.132	0.076	0.115
	trial 2	0.151	0.077	0.144	0.168	0.095	0.119	0.086	0.111
	trial 3	0.204	0.139	0.109	0.093	0.104	0.101	0.077	0.107
	trial 4	0.139	0.130	0.165	0.113	0.117	0.128	0.076	0.108
	average	**0.150**	**0.106**	**0.150**	**0.130**	**0.105**	**0.120**	**0.079**	**0.110**

First Order System Modelling - 2L3LT4ST100I									
Applied Torque (Nm)		0.03		0.05		0.07		0.10	
Direction		CCW	CW	CCW	CW	CCW	CW	CCW	CW
k (Nm/rad)	trial 1	0.414	0.465	0.442	0.458	0.422	0.460	0.404	0.444
	trial 2	0.389	0.441	0.422	0.460	0.422	0.459	0.366	0.436
	trial 3	0.421	0.460	0.411	0.424	0.401	0.437	0.365	0.390
	trial 4	0.404	0.446	0.458	0.458	0.400	0.416	0.374	0.398
	average	**0.407**	**0.453**	**0.434**	**0.450**	**0.411**	**0.443**	**0.377**	**0.417**
b (Nms/rad)	trial 1	0.084	0.094	0.106	0.102	0.091	0.098	0.096	0.098
	trial 2	0.078	0.090	0.086	0.097	0.094	0.077	0.081	0.090
	trial 3	0.096	0.103	0.086	0.091	0.086	0.100	0.083	0.083
	trial 4	0.082	0.095	0.102	0.093	0.087	0.087	0.087	0.093
	average	**0.085**	**0.095**	**0.095**	**0.096**	**0.089**	**0.091**	**0.087**	**0.091**

First Order System Modelling - 2L4LT4ST37T									
Applied Torque (Nm)		0.04		0.10		0.20		0.30	
Direction		CCW	CW	CCW	CW	CCW	CW	CCW	CW
k (Nm/rad)	trial 1	0.897	0.885	0.837	0.853	0.679	0.786	0.499	0.657
	trial 2	0.877	0.907	0.839	0.851	0.672	0.791	0.540	0.662
	trial 3	0.857	0.876	0.826	0.819	0.692	0.782	0.499	0.711
	trial 4	0.922	0.931	0.833	0.833	0.714	0.790	0.540	0.716
	average	**0.888**	**0.900**	**0.834**	**0.839**	**0.689**	**0.787**	**0.519**	**0.686**
b (Nms/rad)	trial 1	0.245	0.221	0.212	0.236	0.174	0.199	0.126	0.160
	trial 2	0.219	0.200	0.210	0.216	0.148	0.200	0.141	0.163
	trial 3	0.206	0.240	0.204	0.186	0.196	0.188	0.126	0.180
	trial 4	0.203	0.189	0.211	0.205	0.171	0.205	0.141	0.188
	average	**0.218**	**0.212**	**0.209**	**0.211**	**0.172**	**0.198**	**0.133**	**0.173**

First Order System Modelling - 2L4LT4ST100I									
Applied Torque (Nm)		0.06		0.10		0.20		0.30	
Direction		CCW	CW	CCW	CW	CCW	CW	CCW	CW
k (Nm/rad)	trial 1	0.988	1.181	1.007	1.085	0.958	1.123	0.622	0.966
	trial 2	1.085	1.105	1.114	1.063	0.897	0.984	0.601	0.848
	trial 3	1.085	1.088	0.987	1.016	0.863	1.005	0.585	0.873
	trial 4	1.105	1.083	1.081	1.031	0.783	1.006	0.582	0.792
	average	**1.066**	**1.114**	**1.047**	**1.049**	**0.875**	**1.030**	**0.597**	**0.870**
b (Nms/rad)	trial 1	0.208	0.240	0.158	0.224	0.217	0.255	0.149	0.200
	trial 2	0.213	0.173	0.238	0.191	0.179	0.236	0.156	0.175
	trial 3	0.217	0.232	0.204	0.234	0.196	0.224	0.150	0.195
	trial 4	0.225	0.224	0.220	0.217	0.185	0.218	0.150	0.190
	average	**0.216**	**0.217**	**0.205**	**0.216**	**0.194**	**0.233**	**0.151**	**0.190**

First Order System Modelling - 2L5LT2ST37T									
Applied Torque (Nm)		0.02		0.04		0.10		0.20	
Direction		CCW	CW	CCW	CW	CCW	CW	CCW	CW
k (Nm/rad)	trial 1	1.041	0.970	0.950	0.995	0.886	0.945	0.588	0.796
	trial 2	0.487	1.041	0.935	0.995	0.823	0.895	0.608	0.805
	trial 3	1.040	1.133	0.988	1.041	0.859	0.891	0.589	0.813
	trial 4	1.004	1.144	0.988	1.004	0.798	0.881	0.597	0.816
	average	**0.893**	**1.072**	**0.965**	**1.009**	**0.841**	**0.903**	**0.596**	**0.807**
b (Nms/rad)	trial 1	0.163	0.217	0.161	0.209	0.192	0.183	0.125	0.188
	trial 2	0.097	0.201	0.115	0.209	0.178	0.200	0.138	0.158
	trial 3	0.215	0.246	0.178	0.215	0.183	0.208	0.120	0.198
	trial 4	0.221	0.225	0.165	0.181	0.112	0.161	0.137	0.188
	average	**0.174**	**0.222**	**0.155**	**0.203**	**0.166**	**0.188**	**0.130**	**0.183**

First Order System Modelling - 2L5LT2ST100I									
Applied Torque (Nm)		0.04		0.08		0.14		0.20	
Direction		CCW	CW	CCW	CW	CCW	CW	CCW	CW
k (Nm/rad)	trial 1	0.829	1.007	0.863	1.032	0.773	1.169	0.680	0.910
	trial 2	0.839	1.212	0.818	1.115	0.785	1.010	0.576	0.754
	trial 3	0.865	1.085	1.089	1.049	0.780	1.015	0.565	0.708
	trial 4	0.836	1.301	0.848	1.035	0.747	1.024	0.575	0.687
	average	**0.842**	**1.151**	**0.905**	**1.058**	**0.771**	**1.055**	**0.599**	**0.765**
b (Nms/rad)	trial 1	0.155	0.175	0.181	0.210	0.178	0.269	0.154	0.197
	trial 2	0.095	0.226	0.186	0.219	0.165	0.202	0.140	0.161
	trial 3	0.147	0.192	0.236	0.220	0.172	0.210	0.136	0.156
	trial 4	0.134	0.243	0.170	0.262	0.162	0.205	0.138	0.156
	average	**0.133**	**0.209**	**0.193**	**0.228**	**0.169**	**0.221**	**0.142**	**0.167**

First Order System Modelling - 2L5LT4ST37T									
Applied Torque (Nm)		0.04		0.08		0.14		0.20	
Direction		CCW	CW	CCW	CW	CCW	CW	CCW	CW
k (Nm/rad)	trial 1	1.416	1.770	1.392	1.789	1.281	1.475	1.073	1.332
	trial 2	1.493	1.957	1.418	1.789	1.332	1.602	1.155	1.427
	trial 3	1.569	2.056	1.458	1.772	1.336	1.600	1.182	1.141
	trial 4	1.533	1.804	1.495	1.789	1.335	1.541	1.157	1.400
	average	**1.503**	**1.897**	**1.441**	**1.785**	**1.321**	**1.555**	**1.142**	**1.325**
b (Nms/rad)	trial 1	0.302	0.266	0.357	0.340	0.320	0.369	0.301	0.346
	trial 2	0.314	0.489	0.383	0.405	0.320	0.475	0.331	0.333
	trial 3	0.361	0.425	0.272	0.437	0.361	0.448	0.343	0.327
	trial 4	0.281	0.379	0.339	0.423	0.338	0.421	0.293	0.331
	average	**0.314**	**0.390**	**0.338**	**0.402**	**0.335**	**0.428**	**0.317**	**0.334**

First Order System Modelling - 2L5LT4ST100I									
Applied Torque (Nm)		0.06		0.12		0.20		0.30	
Direction		CCW	CW	CCW	CW	CCW	CW	CCW	CW
k (Nm/rad)	trial 1	1.670	2.241	1.820	2.695	1.850	2.396	1.578	2.176
	trial 2	1.483	2.245	2.291	2.300	1.955	2.217	1.721	1.967
	trial 3	1.499	2.391	1.785	2.484	1.697	2.067	1.503	1.923
	trial 4	1.369	2.464	1.751	2.451	1.676	2.158	1.465	1.934
	average	**1.505**	**2.335**	**1.912**	**2.483**	**1.795**	**2.210**	**1.567**	**2.000**
b (Nms/rad)	trial 1	0.323	0.448	0.413	0.494	0.395	0.423	0.342	0.486
	trial 2	0.267	0.516	0.535	0.353	0.463	0.503	0.407	0.367
	trial 3	0.230	0.438	0.315	0.364	0.322	0.338	0.341	0.404
	trial 4	0.214	0.197	0.379	0.327	0.279	0.496	0.337	0.355
	average	**0.259**	**0.400**	**0.410**	**0.384**	**0.365**	**0.440**	**0.357**	**0.403**

First Order System Modelling - 2L5LT8ST37T									
Applied Torque (Nm)		0.08		0.14		0.24		0.34	
Direction		CCW	CW	CCW	CW	CCW	CW	CCW	CW
k (Nm/rad)	trial 1	2.365	2.464	2.306	2.806	1.872	2.244	1.808	2.027
	trial 2	2.758	2.679	2.627	2.839	2.178	2.706	2.302	2.303
	trial 3	2.444	2.679	2.586	2.914	2.864	2.643	2.322	2.594
	trial 4	2.424	2.618	2.410	2.803	3.002	2.659	2.370	2.590
	average	**2.498**	**2.610**	**2.482**	**2.840**	**2.479**	**2.563**	**2.200**	**2.379**
b (Nms/rad)	trial 1	0.410	0.394	0.354	0.571	0.281	0.359	0.259	0.372
	trial 2	0.386	0.437	0.534	0.530	0.290	0.478	0.414	0.415
	trial 3	0.448	0.455	0.448	0.495	0.554	0.476	0.410	0.458
	trial 4	0.444	0.506	0.410	0.476	0.500	0.452	0.419	0.458
	average	**0.422**	**0.448**	**0.436**	**0.518**	**0.406**	**0.441**	**0.376**	**0.426**

First Order System Modelling - 2L5LT8ST100I									
Applied Torque (Nm)		0.10		0.20		0.40		0.858	
Direction		CCW	CW	CCW	CW	CCW	CW	CCW	CW
k (Nm/rad)	trial 1	3.946	3.782	3.918	4.195	3.719	4.220	3.436	4.524
	trial 2	3.717	3.600	3.958	3.936	3.707	4.024	3.044	3.544
	trial 3	3.802	3.584	3.836	3.879	3.596	3.919	3.012	3.385
	trial 4	3.856	3.730	3.763	3.893	3.485	4.013	2.943	3.422
	average	**3.830**	**3.674**	**3.869**	**3.976**	**3.627**	**4.044**	**3.109**	**3.719**
b (Nms/rad)	trial 1	0.815	0.794	0.771	0.867	0.781	0.788	1.008	1.041
	trial 2	0.632	0.672	0.818	0.814	0.840	0.818	0.903	0.827
	trial 3	0.824	0.729	0.818	0.672	0.827	0.888	0.914	0.790
	trial 4	0.835	0.796	0.803	0.740	0.825	0.910	0.883	0.798
	average	**0.777**	**0.748**	**0.802**	**0.773**	**0.818**	**0.851**	**0.927**	**0.864**

First Order System Modelling - 2L5LT12ST37T									
Applied Torque (Nm)		0.245		0.429		0.613		0.858	
Direction		CCW	CW	CCW	CW	CCW	CW	CCW	CW
k (Nm/rad)	trial 1	3.663	3.549	3.386	3.340	2.828	3.095	2.521	2.875
	trial 2	3.657	3.725	3.491	3.532	3.279	3.423	2.973	3.318
	trial 3	3.715	3.676	3.517	3.620	3.285	3.756	2.960	3.368
	trial 4	3.676	3.638	3.522	3.636	3.234	3.540	2.939	3.352
	average	**3.678**	**3.647**	**3.479**	**3.532**	**3.157**	**3.454**	**2.849**	**3.228**
b (Nms/rad)	trial 1	0.635	0.615	0.677	0.646	0.660	0.887	0.664	0.815
	trial 2	0.622	0.633	0.908	0.671	0.743	0.753	0.773	0.796
	trial 3	0.619	0.625	0.703	0.688	0.745	0.839	0.770	0.808
	trial 4	0.600	0.594	0.704	0.727	0.722	0.791	0.764	0.782
	average	**0.619**	**0.617**	**0.748**	**0.683**	**0.717**	**0.817**	**0.743**	**0.800**

First Order System Modelling - 2L5LT12ST100I									
Applied Torque (Nm)		0.245		0.613		0.858		1.226	
Direction		CCW	CW	CCW	CW	CCW	CW	CCW	CW
k (Nm/rad)	trial 1	5.371	5.508	4.473	4.678	3.661	3.734	2.995	3.586
	trial 2	5.518	5.373	3.952	3.947	3.547	3.456	3.593	3.049
	trial 3	5.507	5.122	3.905	3.810	3.438	3.456	2.880	3.026
	trial 4	5.227	5.122	3.805	3.856	3.401	3.350	2.756	2.811
	average	**5.406**	**5.281**	**4.034**	**4.073**	**3.512**	**3.499**	**3.056**	**3.118**
b (Nms/rad)	trial 1	0.770	1.102	0.626	0.889	0.964	0.846	0.869	1.052
	trial 2	0.791	1.057	0.817	0.763	0.981	0.772	1.030	0.904
	trial 3	0.771	1.024	0.768	0.749	0.928	0.772	0.826	0.888
	trial 4	0.993	1.024	1.027	0.758	0.918	0.759	0.818	0.843
	average	**0.831**	**1.052**	**0.810**	**0.790**	**0.948**	**0.787**	**0.885**	**0.922**

Appendix C: Spring Parameters – Conservation of Energy

Table C-1: Spring parameters calculated through conservation of energy for springs with 37% triangular infill and constant spring thickness

Fixed Spring Thickness 4mm 37T			
Spring Leg Width	**Direction**	**k (Nm/rad)**	**b (Nms/rad)**
2	CCW	0.0508	0.0260
	CW	0.0734	0.0456
3	CCW	0.1953	0.0812
	CW	0.1943	0.1146
4	CCW	0.4027	0.2054
	CW	0.4261	0.2067
5	CCW	0.7284	0.3539
	CW	0.7633	0.4340

Table C-2: Spring parameters calculated through conservation of energy for springs with 37% triangular infill and constant spring leg width

Fixed Spring Leg Width 5mm 37T			
Spring Thickness	**Direction**	**k (Nm/rad)**	**b (Nms/rad)**
2	CCW	0.3294	0.0842
	CW	0.3999	0.2038
4	CCW	0.7284	0.3539
	CW	0.7633	0.4340
8	CCW	1.2469	0.7061
	CW	1.2942	0.9117
12	CCW	3.9859	0.6547
	CW	4.3575	0.8036

Table C-3: Spring parameters calculated through conservation of energy for springs with 100% infill and constant spring thickness

Fixed Spring Thickness 4mm 100I			
Spring Leg Width	**Direction**	**k (Nm/rad)**	**b (Nms/rad)**
2	CCW	0.0726	0.0360
	CW	0.0821	0.0498
3	CCW	0.1790	0.0960
	CW	0.2125	0.1495
4	CCW	0.4866	0.2369
	CW	0.5662	0.2922
5	CCW	1.0669	0.5116
	CW	1.0686	0.6851

Table C-4: Spring parameters calculated through conservation of energy for springs with 100% infill and constant spring leg width

Fixed Spring Leg Width 5mm 100I			
Spring Thickness	**Direction**	**k (Nm/rad)**	**b (Nms/rad)**
2	CCW	0.4878	0.2844
	CW	0.4980	0.2719
4	CCW	1.0669	0.5116
	CW	1.0686	0.6851
8	CCW	2.2482	1.3748
	CW	2.4959	1.8942
12	CCW	9.1258	1.5415
	CW	10.0171	2.0675

Table C-5: Spring parameters calculated through conservation of energy modelling

Conservation of Energy Modelling - 2L2LT4ST37T							
Applied Torque (Nm)		0.01		0.02		0.04	
Direction		CCW	CW	CCW	CW	CCW	CW
k (Nm/rad)	trial 1	0.064	0.074	0.055	0.070	0.049	0.067
	trial 2	0.073	0.083	0.062	0.079	0.053	0.074
	trial 3	0.079	0.086	0.062	0.087	0.051	0.076
	trial 4	0.080	0.076	0.060	0.087	0.051	0.077
	average	**0.074**	**0.080**	**0.060**	**0.081**	**0.051**	**0.073**
b (Nms/rad)	trial 1	0.021	0.033	0.023	0.047	0.026	0.044
	trial 2	0.021	0.035	0.022	0.044	0.026	0.046
	trial 3	0.021	0.035	0.025	0.044	0.027	0.046
	trial 4	0.021	0.032	0.021	0.044	0.026	0.046
	average	**0.021**	**0.034**	**0.023**	**0.045**	**0.026**	**0.046**

Conservation of Energy Modelling - 2L2LT4ST100I							
Applied Torque (Nm)		0.01		0.02		0.04	
Direction		CCW	CW	CCW	CW	CCW	CW
k (Nm/rad)	trial 1	0.075	0.082	0.063	0.081	0.067	0.078
	trial 2	0.086	0.099	0.079	0.090	0.073	0.086
	trial 3	0.093	0.114	0.082	0.095	0.076	0.081
	trial 4	0.100	0.111	0.082	0.093	0.074	0.083
	average	**0.088**	**0.101**	**0.076**	**0.089**	**0.073**	**0.082**
b (Nms/rad)	trial 1	0.027	0.038	0.030	0.047	0.036	0.049
	trial 2	0.028	0.045	0.032	0.047	0.036	0.053
	trial 3	0.027	0.039	0.031	0.049	0.036	0.048
	trial 4	0.027	0.039	0.031	0.055	0.036	0.050
	average	**0.027**	**0.040**	**0.031**	**0.049**	**0.036**	**0.050**

Conservation of Energy Modelling - 2L3LT4ST37T							
Applied Torque (Nm)		0.01		0.02		0.04	
Direction		CCW	CW	CCW	CW	CCW	CW
k (Nm/rad)	trial 1	0.353	0.480	0.157	0.154	0.150	0.169
	trial 2	0.802	0.498	0.229	0.198	0.203	0.198
	trial 3	1.135	0.503	0.246	0.211	0.208	0.206
	trial 4	0.932	0.470	0.245	0.215	0.220	0.205
	average	**0.805**	**0.488**	**0.219**	**0.195**	**0.195**	**0.194**
b (Nms/rad)	trial 1	0.284	0.383	0.076	0.126	0.077	0.140
	trial 2	0.305	0.987	0.074	0.106	0.082	0.106
	trial 3	0.258	0.285	0.073	0.133	0.082	0.111
	trial 4	0.278	0.285	0.078	0.126	0.084	0.102
	average	**0.281**	**0.485**	**0.075**	**0.123**	**0.081**	**0.115**

Conservation of Energy Modelling - 2L3LT4ST100I							
Applied Torque (Nm)		0.02		0.04		0.10	
Direction		CCW	CW	CCW	CW	CCW	CW
k (Nm/rad)	trial 1	0.241	0.210	0.169	0.237	0.165	0.204
	trial 2	0.231	0.264	0.211	0.247	0.184	0.216
	trial 3	0.249	0.261	0.222	0.245	0.184	0.215
	trial 4	0.248	0.289	0.224	0.241	0.183	0.216
	average	**0.242**	**0.256**	**0.206**	**0.242**	**0.179**	**0.213**
b (Nms/rad)	trial 1	0.079	0.145	0.086	0.118	0.100	0.145
	trial 2	0.080	0.138	0.088	0.125	0.097	0.144
	trial 3	0.084	0.144	0.083	0.131	0.097	0.150
	trial 4	0.077	0.149	0.088	0.122	0.091	0.160
	average	**0.080**	**0.144**	**0.086**	**0.124**	**0.096**	**0.149**

Conservation of Energy Modelling - 2L4ST4LT37T							
Applied Torque (Nm)		0.02		0.04		0.10	
Direction		CCW	CW	CCW	CW	CCW	CW
k (Nm/rad)	trial 1	0.356	0.550	0.317	0.375	0.324	0.362
	trial 2	0.513	0.600	0.461	0.476	0.420	0.443
	trial 3	0.534	0.594	0.484	0.507	0.433	0.448
	trial 4	0.569	0.634	0.502	0.512	0.434	0.452
	average	**0.493**	**0.594**	**0.441**	**0.468**	**0.403**	**0.426**
b (Nms/rad)	trial 1	0.257	0.288	0.185	0.234	0.198	0.218
	trial 2	0.223	0.298	0.198	0.216	0.207	0.195
	trial 3	0.220	0.310	0.196	0.267	0.209	0.201
	trial 4	0.225	0.281	0.207	0.219	0.208	0.212
	average	**0.231**	**0.294**	**0.196**	**0.234**	**0.205**	**0.207**

Conservation of Energy Modelling - 2L4LT4ST100I							
Applied Torque (Nm)		0.02		0.04		0.10	
Direction		CCW	CW	CCW	CW	CCW	CW
k (Nm/rad)	trial 1	0.414	0.497	0.395	0.520	0.402	0.486
	trial 2	0.523	0.621	0.510	0.631	0.498	0.588
	trial 3	0.605	0.747	0.521	0.652	0.518	0.590
	trial 4	0.591	0.653	0.598	0.697	0.529	0.602
	average	**0.533**	**0.629**	**0.506**	**0.625**	**0.487**	**0.566**
b (Nms/rad)	trial 1	0.297	0.521	0.233	0.347	0.233	0.297
	trial 2	0.292	0.459	0.241	0.336	0.232	0.282
	trial 3	0.328	0.369	0.224	0.374	0.236	0.292
	trial 4	0.288	0.374	0.287	0.334	0.246	0.299
	average	**0.301**	**0.431**	**0.246**	**0.348**	**0.237**	**0.292**

Conservation of Energy Modelling - 2L5LT2ST37T							
Applied Torque (Nm)		0.01		0.02		0.04	
Direction		CCW	CW	CCW	CW	CCW	CW
k (Nm/rad)	trial 1	0.290	0.308	0.337	0.261	0.237	0.363
	trial 2	0.341	0.332	0.447	0.426	0.343	0.398
	trial 3	0.408	0.468	0.400	0.478	0.365	0.424
	trial 4	0.464	0.544	0.437	0.449	0.373	0.415
	average	**0.376**	**0.413**	**0.405**	**0.403**	**0.329**	**0.400**
b (Nms/rad)	trial 1	0.417	1.005	0.191	0.234	0.096	0.208
	trial 2	0.332	0.324	0.187	0.266	0.079	0.194
	trial 3	0.238	0.280	0.192	0.228	0.078	0.212
	trial 4	0.294	0.286	0.194	0.254	0.084	0.201
	average	**0.320**	**0.474**	**0.191**	**0.245**	**0.084**	**0.204**

Conservation of Energy Modelling - 2L5LT2ST100I							
Applied Torque (Nm)		0.01		0.02		0.04	
Direction		CCW	CW	CCW	CW	CCW	CW
k (Nm/rad)	trial 1	0.482	0.457	0.339	0.416	0.324	0.363
	trial 2	0.716	0.791	0.503	0.582	0.523	0.507
	trial 3	0.587	0.769	0.566	0.629	0.558	0.539
	trial 4	0.678	0.730	0.639	0.732	0.546	0.584
	average	**0.616**	**0.687**	**0.512**	**0.590**	**0.488**	**0.498**
b (Nms/rad)	trial 1	0.367	1.036	0.248	0.358	0.256	0.265
	trial 2	0.403	0.428	0.288	0.346	0.282	0.282
	trial 3	0.287	0.459	0.250	0.355	0.310	0.269
	trial 4	0.350	0.429	0.266	0.439	0.290	0.272
	average	**0.352**	**0.588**	**0.263**	**0.374**	**0.284**	**0.272**

Conservation of Energy Modelling - 2L5LT4ST37T							
Applied Torque (Nm)		0.02		0.04		0.10	
Direction		CCW	CW	CCW	CW	CCW	CW
k (Nm/rad)	trial 1	0.435	1.442	0.416	0.526	0.508	0.570
	trial 2	1.037	1.864	0.789	1.064	0.796	0.813
	trial 3	0.936	0.518	0.826	1.021	0.798	0.832
	trial 4	1.037	1.419	0.867	1.044	0.812	0.837
	average	**0.861**	**1.311**	**0.724**	**0.914**	**0.728**	**0.763**

b (Nms/rad)	trial 1	0.565	0.771	0.336	0.548	0.324	0.447
	trial 2	0.476	0.686	0.357	0.488	0.367	0.403
	trial 3	0.611	0.640	0.329	0.513	0.364	0.415
	trial 4	0.541	0.744	0.354	0.541	0.360	0.471
	average	**0.548**	**0.710**	**0.344**	**0.522**	**0.354**	**0.434**

Conservation of Energy Modelling - 2L5LT4ST100I							
Applied Torque (Nm)		0.02		0.04		0.10	
Direction		CCW	CW	CCW	CW	CCW	CW
k (Nm/rad)	trial 1	0.758	1.188	0.660	0.885	0.829	0.926
	trial 2	1.253	1.239	1.138	1.149	1.128	1.103
	trial 3	1.295	1.626	1.161	1.269	1.134	1.105
	trial 4	1.239	1.442	1.203	1.210	1.177	1.140
	average	**1.136**	**1.374**	**1.040**	**1.128**	**1.067**	**1.069**

b (Nms/rad)	trial 1	1.026	1.239	0.536	0.862	0.523	0.810
	trial 2	1.023	1.013	0.564	0.812	0.505	0.625
	trial 3	0.855	1.410	0.527	0.761	0.508	0.632
	trial 4	1.185	1.332	0.560	0.745	0.511	0.674
	average	**1.022**	**1.248**	**0.547**	**0.795**	**0.512**	**0.685**

Conservation of Energy Modelling - 2L5LT8ST37T							
Applied Torque (Nm)		0.04		0.10		0.20	
Direction		CCW	CW	CCW	CW	CCW	CW
k (Nm/rad)	trial 1	1.655	2.590	1.022	1.254	1.064	0.989
	trial 2	1.643	2.277	1.765	1.590	1.272	1.378
	trial 3	1.679	2.056	1.581	1.654	1.321	1.425
	trial 4	1.871	2.038	1.683	1.698	1.330	1.385
	average	**1.712**	**2.240**	**1.513**	**1.549**	**1.247**	**1.294**
b (Nms/rad)	trial 1	1.265	1.936	0.965	1.444	0.692	0.875
	trial 2	1.068	1.341	0.985	1.102	0.687	0.928
	trial 3	1.029	1.135	0.735	1.080	0.706	0.985
	trial 4	1.226	1.328	0.716	1.042	0.740	0.859
	average	**1.147**	**1.435**	**0.850**	**1.167**	**0.706**	**0.912**

Conservation of Energy Modelling - 2L5LT8ST100I							
Applied Torque (Nm)		0.04		0.10		0.20	
Direction		CCW	CW	CCW	CW	CCW	CW
k (Nm/rad)	trial 1	1.746	4.358	1.685	2.101	1.829	2.160
	trial 2	2.224	3.447	2.369	2.623	2.321	2.467
	trial 3	2.533	3.728	2.508	3.076	2.366	2.675
	trial 4	2.728	5.152	2.383	3.024	2.478	2.681
	average	**2.308**	**4.171**	**2.236**	**2.706**	**2.248**	**2.496**
b (Nms/rad)	trial 1	4.423	5.193	1.950	3.092	1.451	1.918
	trial 2	3.464	3.448	1.695	2.312	1.377	1.797
	trial 3	3.215	3.889	1.651	2.525	1.339	1.776
	trial 4	3.221	3.831	1.531	2.810	1.333	2.086
	average	**3.581**	**4.090**	**1.706**	**2.685**	**1.375**	**1.894**

Conservation of Energy Modelling - 2L5LT12ST37T							
Applied Torque (Nm)		0.123		0.245		0.613	
Direction		CCW	CW	CCW	CW	CCW	CW
k (Nm/rad)	trial 1	5.160	5.555	4.661	4.626	3.530	4.192
	trial 2	4.756	5.343	5.587	4.931	4.024	4.321
	trial 3	6.660	5.555	5.436	5.554	4.182	4.498
	trial 4	5.131	5.930	4.303	5.343	4.207	4.419
	average	**5.427**	**5.595**	**4.997**	**5.113**	**3.986**	**4.358**

b (Nms/rad)	trial 1	2.657	1.962	1.298	1.359	0.689	0.876
	trial 2	1.816	1.790	1.273	1.397	0.652	0.779
	trial 3	2.449	1.814	1.307	1.396	0.644	0.778
	trial 4	1.991	1.859	1.252	1.339	0.634	0.781
	average	**2.228**	**1.856**	**1.283**	**1.373**	**0.655**	**0.804**

Conservation of Energy Modelling - 2L5LT12ST100I							
Applied Torque (Nm)		0.123		0.245		0.613	
Direction		CCW	CW	CCW	CW	CCW	CW
k (Nm/rad)	trial 1	10.488	9.909	9.927	10.315	8.750	9.920
	trial 2	9.921	10.489	10.577	10.871	9.291	9.837
	trial 3	10.661	11.050	10.890	11.651	9.005	9.982
	trial 4	11.282	11.237	10.719	11.256	9.457	10.330
	average	**10.588**	**10.671**	**10.528**	**11.023**	**9.126**	**10.017**

b (Nms/rad)	trial 1	4.321	5.913	3.183	3.900	1.553	2.085
	trial 2	4.158	5.347	3.190	3.526	1.565	2.053
	trial 3	4.712	5.425	3.154	3.732	1.506	2.091
	trial 4	4.781	5.132	3.031	3.920	1.542	2.041
	average	**4.493**	**5.454**	**3.139**	**3.769**	**1.541**	**2.067**